HIGH-THROUGHPUT CELL ENCAPSULATION IN MONODISPERSE AGAROSE MICROCAPSULES USING A MICROFLUIDIC DEVICE

NICOLAS MONETTE-CATAFARD

THESIS SUBMITTED IN PARTIAL FULFILLMENT OF THE REQUIRMENTS FOR THE DEGREE OF

MASTER OF SCIENCE

In the Faculty of Graduate Studies (Physics)

STATEMENT OF ORIGINALITY

To the best of the author's knowledge, the content presented in this thesis is the product of original work done by the author at the University of Ottawa under the supervision of Professor Michel Godin.

As partial requirement for the degree of Master of Science (Physics) at the University of Ottawa, research on cell encapsulation within agarose microcapsules using a microfluidic device was presented at the Ottawa Carleton Institute of Physics symposium:

Nicolas M Catafard and Michel Godin, *Cell encapsulation into monodisperse picoliter microgels using a microfluidic device.* Ottawa Carleton Institute of Physics (May 2014).

A presentation on the same topic was also given at the Novel Cardiovascular Repair using Enhanced Stem-Cell Therapy Scientific Meeting:

Nicolas M Catafard and Michel Godin, *Cell encapsulation into monodisperse picoliter microgels using a microfluidic device.* Novel Cardiovascular Repair using Enhanced Stem-Cell Therapy Scientific Meeting (Mars 2014).

STATEMENT OF CONTRIBUTIONS

All design, microfabrication and sample preparation were performed by the author. All data acquisition and analysis were also performed by the author, with the exception of image acquisition with a confocal microscope and subsequent image processing, which was performed by Daniel Modulevsky (PhD candidate, University of Ottawa). Some of the cells used were partially processed by Dr. Benjamin Watts (Postdoctoral fellow, University of Ottawa). The LabVIEW program used for image acquisition was developed by Lukasz Andrzejewski, while those for pneumatic and temperature control were originally developed by Michel Godin and adapted by the author. All figures and tables were prepared by the author, with the exception of Figure 1.1b, 1.2, 2.1,2.2 and 2.3, which were adapted from already published material (the source is explicitly mentioned in the caption), and Figure 7.8, which was provided by Daniel Modulevsky. A request for the written authorization to use all published material has been sent

CONTENTS

LIST OF FIGURES

LIST OF TABLES

ACKNOWLEDGEMENTS

First and foremost, I would like to thank my supervisor Dr. Michel Godin. His continuous presence and expert advice provided me with plentiful resources to overcome the many adversities encountered during this project. Furthermore, his patience and understanding of my specific situation always gave me confidence in the quality of my results and strength to pursue my research.

The multidisciplinarity of the project prompted many conceptual and technical challenges related to different fields. I would like to thank Dr. Duncan Stewart and Dr. David Courtman for their precious expertise in cell-based therapy. I would like to thank Dr. Benjamin Watts for his advice in microfabrication and for the numerous discussions we had concerning interpretation of the results. I would also like to thank Daniel Modulevsky, whose expertise in microbiology and confocal microscopy helped a physicist find his way in a cell culture room, and Eric Beamish, with whom I have discussed many issues related to surface chemistry. Special thanks to Radin Tahvildari, Daniel Sigouin, Dr. Jason Riordon and all of the other lab members for the fruitful discussions and for creating a positive work environment.

Most importantly, I would like to thank my wife, Anny Lachance. Without your unconditional love and support, none of this would have been possible.

ABSTRACT

Over the last decade, microfluidics has emerged as a distinct new field with promising applications for diverse research areas. The ability to precisely control fluids at the microscale allows the execution of a variety of programmable semi-automatic operations on the same device, effectively forming a lab-on-a-chip. In particular, droplet-based microfluidic systems – which reliably generate highly uniform microdroplets at a high throughput – enable the controlled compartmentalization of biological material and have the potential to influence mainstream biomedical research. In this thesis, a microfluidic platform is presented that allows the encapsulation of viable cells in agarose microcapsules for applications in cell–based therapy. As an improvement to pre-existing methods of cell encapsulation, the proposed system combines continuous high throughput cell-encapsulation with on-chip microcapsule gelation and purification.

Chapter 1 INTRODUCTION

Cell-based therapy[1] is an intense area of research with promising applications for the treatment of many human pathological conditions. The natural regeneration process of mammalian adults relies on the self-renewal of differentiated cells in the case of a minor injury, whereas new populations of cells are derived from multipotent[2] stem cells or progenitor cells in the case of a major injury. In an adult body however, these multipotent cells are in a quiescent non-dividing state and their differentiation requires environmental stimuli that are usually lacking. Consequently, the ability of mature tissues to self-repair is compromised. In this case, cell implants can enhance the healing process by either secreting missing factors or active substances, playing a specific physiological role, or replacing and reconstructing damaged tissues[1]. The most famous example is bone marrow cell transplant for cancer patients, which allows the patients to reconstitute their immune system impaired by chemotherapy and radiation[2]. Many other applications have been demonstrated such as the treatment of heart diseases[3], the salvation of ischemic limb vasculature[4] or the improvement of motor function in Parkinson's disease[5].

Unfortunately, the choice of the cell source for implantation is severely limited by the availability of the cells and their ability to multiply *in vitro*. In many cases, non-autologous cells[3] must be used, which causes an immunological response that threatens to destroy the implanted cells. To overcome this, immunosuppression is traditionally used but can severely compromise the immune system's ability to fight infectious disease[6]. Furthermore, the retention of the cells in the host system is typically very low and must be compensated by injecting many more cells than are actually needed for the treatment[7].

To increase cell viability and retention, cell encapsulation – the immobilization of cells within micron-sized spherical microcapsules comprised of a semipermeable polymer matrix – is a very promising strategy that has been gaining popularity ever since the pioneer work of TMS Chang[8] in the early 1960s (see *Figure 1-1*a). The main idea is that the semipermeable matrix surrounding the cell selectively blocks the diffusion of molecules based on their molecular weight. Smaller molecules such as nutrients, oxygen, growth factors and cell secretions can freely diffuse in or out of the capsule, whereas larger entities such as immune cells are excluded[9] (see *Figure 1-1*b).

[1] The injection of living cells into a patient, aiming to replace or repair the biological function of a damaged tissue or organ
[2] Cells that have the ability to differentiate into many different cell types
[3] Cells that do not come from the same individual

Using this technique, enhanced transplanted cell survival and retention in the absence of immunosuppression has been demonstrated for the treatment of many diseases including diabetes[10], hypoparathyroidism[11], dwarfism and hemophilia[12], and central nervous system malignancies[13].

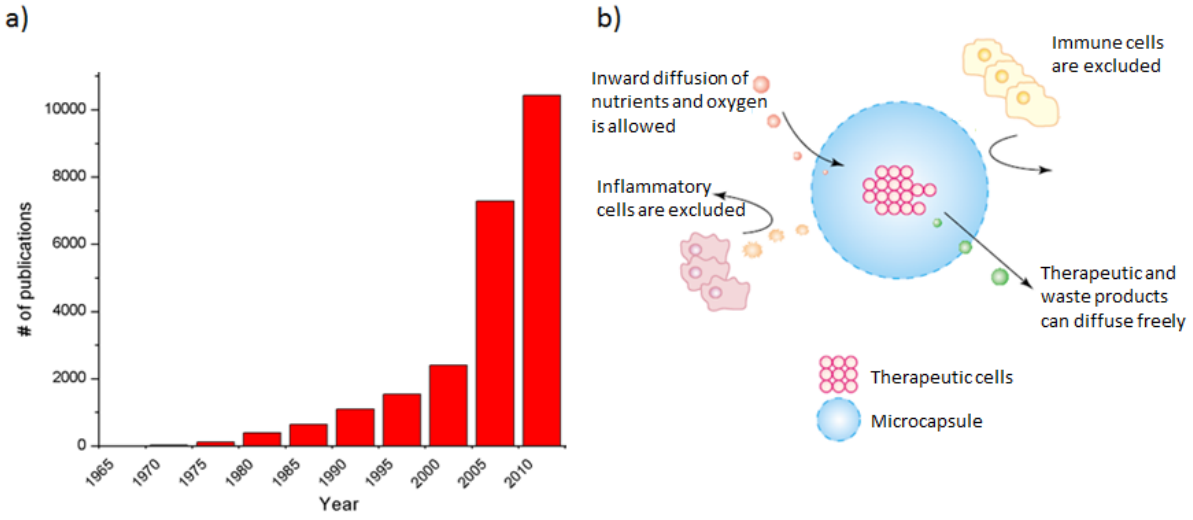

Figure 1-1 a) Number of publications on the topic of "cell encapsulation" for the year 1965 up until today (all databases were accessed via Web of Science); b) schematic of the principle of cell encapsulation: the semipermeable polymer network selectively allows the bi-directional diffusion of oxygen, therapeutic products and waste, while blocking immunoglobins and immune cells.

The design of the microcapsule must take many factors into account: all materials used must be totally biocompatible so that they do not interfere with the homeostasis of the encapsulated cells and surrounding host tissues and do not trigger an immune response in the host; the microcapsules must be mechanically strong enough to withstand physical and osmotic stresses without being deformed or damaged as this would expose the cells to the immune system; the microcapsules permeability and size must be tuned to optimize their diffusion properties (a larger surface-to-volume ratio causes a faster secretory response to external stimuli); and the encapsulation technique must be gentle to preserve cell integrity during and after the transplantation [14].

The properties of several natural and synthetic hydrogels [4] have been studied as biomaterials for the microcapsules since they provide a highly hydrated microenvironment that supports the embedded cell differentiation, proliferation and migration[15]. In general, synthetic

[4] Polymer gels that swell in water without dissolving

polymers offer a greater design flexibility and batch-to-batch uniformity, but are hard to functionalize to promote the interaction of the cell with the polymer network[16]. Consequently, most groups use natural polysaccharides such as alginate and agarose[5] because of their great biocompatibility, mild gelation conditions and the ease with which they can be functionalized to simulate the normal environment of the cell[17]. Alginate is the most popular candidate, although many groups[18–20] now turn to agarose because of its enhanced durability and stability, well characterized properties, extensive use in cell culture and gentler gelation mechanism[14].

Agarose is a thermoreversible gel that transitions from a random coil configuration (in its sol state) to bundles of double helices cross-linked via non-covalent hydrogen bonding (in its gel state)[21,22]. Agarose shows considerable thermal hysteresis[6], with a gelation temperature (ie. the temperature at which it transitions from sol state to gel state) and a melting temperature (ie. the temperature at which it transitions from gel state to sol state) around 40°C and 90°C respectively. However, synthetic hydroxyethylation of agarose is used commercially to decrease the gelation and melting temperature as low as 17°C and 50°C respectively. This engineered ultra-low gelling agarose is ideal for cell encapsulation. It allows the cells to be encapsulated at 37°C in a liquid solution, which is subsequently cooled to obtain gelation, and brought back to 37°C while still remaining in a gel state.

In biomedical research, the most commonly used techniques to produce an emulsion[7] for cell encapsulation can be divided in two broad categories: emulsification and extrusion[14]. With the emulsification method, the polymer solution containing the cells is mixed with an immiscible organic phase and a surfactant, and is dispersed by mechanical stirring. The gelation is initiated by cooling the solution, while the suspended cells are naturally encapsulated in the newly formed microcapsules. This method produces microcapsules with a diameter ranging from hundreds of microns to millimeters with a large size polydispersity[8] (see ***Figure 1-2***a). With the extrusion method, the polymer solution containing the cells is extruded through a small needle or capillary into a gelation bath cooled to the appropriate temperature. This approach is also limited to larger polydisperse microcapsule diameters (0.5 – 3 mm). The challenge is thus to produce small and uniform microcapsules to optimize and regulate their diffusive properties.

[5] An alternating copolymer of 3-linked β-D-galactopyranose and 4-linked 3,6-anhydro-α-L-galactopyranose.
[6] The sol-gel transition temperature differs upon heating or cooling
[7] The mixture of two immiscible fluids: one fluid (ie. the dispersed phase) is dispersed in the other (ie. the continuous phase)
[8] The ratio of the standard deviation of the microcapsule diameter to the mean (also named coefficient of variation)

A vast number of improvements to the conventional methods have been proposed to overcome these issues such as electrospray[23], microthread generation[24], membrane emulsification[25], capillary flow focusing[26] and coflowing stream[27]. The two last techniques offer a particularly great level of control over the size and the uniformity of the microcapsules (see ***Figure 1-2***b).

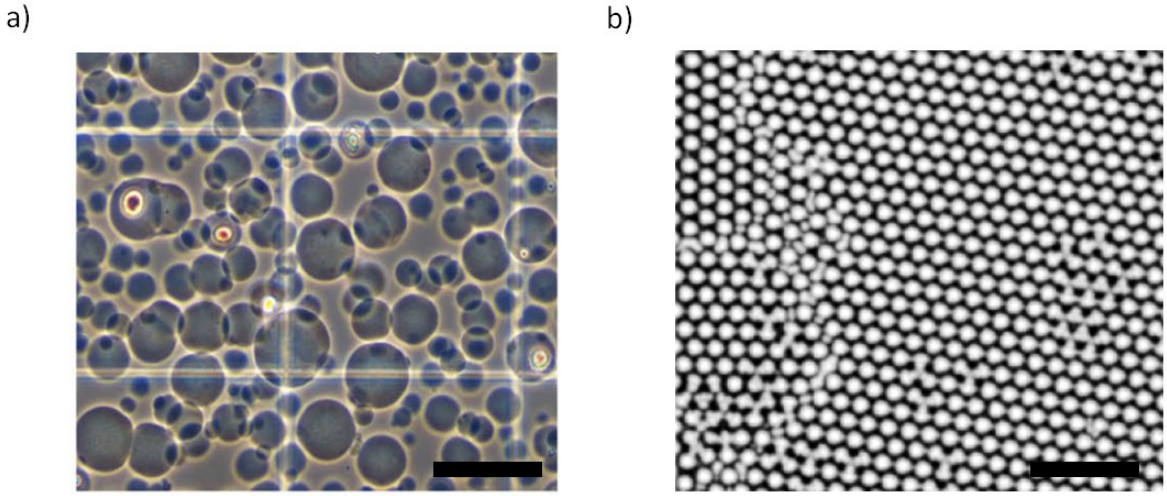

Figure 1-2 a) *Polydisperse microcapsules generated using the conventionnal bulk emulsification method (scale bar = 125 um); b) monodisperse microcapsules generated using the coflowing stream method (scale bar = 60um)*

Microfluidics[9] is undoubtedly a very promising emerging tool to push the emulsion technology even further[28]. Because of the small amounts of fluids involved (typically from nL to aL), inertial forces due to the fluid momentum are typically very small compared to viscous forces which causes the flow to be laminar[10] (low Reynolds numbers). The absence of turbulence allows the precise manipulation of fluids via different microscale geometries and ultimately makes it possible to control the deformation and the breakup of a fluid into monodisperse microdroplets uniform in size (with a coefficient of variation smaller than 3%[29]). However, the real advantage of using microfluidics (as opposed to macroscale techniques such as capillary flow focusing and coflowing stream) is that it opens the possibility for reliable semi-automatic upstream and downstream manipulation of the individual microdroplets such as cell transfection[30], on-demand droplet polymerization[31,32], coalescence[33–35], splitting[36,37], mixing[38], purification[39,40] and sorting[41–43].

[9] The precise control of fluids in channels with dimensions of tens of um
[10] Fluids flow in parallel layers without eddies or turbulence

Furthermore, the microfabrication techniques used to fabricate microfluidic devices allow the rapid prototyping of different designs at a very low cost and reagent consumption.

The production of agarose microcapsules via a microfluidic platform has already been demonstrated for the encapsulation of bacteria[44], yeast cells[45], cancer cells[46], blood progenitor cells[47], and mouse embryonic stem cells[48], as well as for genetic assays[49–52]. Most of these studies perform cell encapsulation on-chip and microcapsule gelation off-chip, while some groups use different trapping systems to allow on-chip microcapsule gelation at the expense of interrupting the microdroplet production[46,52].

A continuous process including uninterrupted production of cell-laden agarose microcapsules with subsequent on-chip gelation is highly desirable for the integration of lab-on-a-chip downstream processing such as sorting and purification of the microcapsules. To my knowledge, this process has never been demonstrated. The continuous flow gelation of agarose microcapsule has been demonstrated[32], but the process relies on regular agarose with a gelation temperature of ~37°C, which is not compatible with cell encapsulation. The goal of this thesis is thus to demonstrate the feasibility of such a system and its relevance to therapeutic applications. In order to meet these requirements, the proposed method: 1) produces agarose microcapsules uniform in shape and in size; 2) encapsulates cells while maintaining their viability; 3) grants control over the number of encapsulated cells per microdroplet; and 4) generates cell-laden microcapsules at a therapeutically relevant rate. As a proof-of-concept that the platform is compatible with additional on-chip downstream processing, on-chip purification of the microcapsules is also demonstrated.

Chapter 2 details the fundamental notions related to cell encapsulation in droplet-based microfluidics, including the methods typically used to produce and collect the cell-laden microcapsules as well as the basic physical and statistical tools to describe microcapsule formation and cell encapsulation. Chapter 3 describes the different microfluidic designs tested, the temperature control system used to obtain on-chip gelation of the agarose microcapsules, as well as the different reagents and methods used to fabricate and operate the system. Chapters 4 to 7 present a detailed discussion on the results obtained with the proposed platform, including high-throughput generation of monodisperse microdroplets (Chapter 4), continuous on-chip microcapsule gelation (Chapter 5), controlled and viable cell encapsulation (Chapter 6) and on-chip microcapsule purification (Chapter 7).

Chapter 2 FUNDAMENTALS OF DROPLET MICROFLUIDICS

2.1 Device geometry

In droplet microfluidics, passive methods to generate microdroplets are typically based on one of two main geometries[29]: a coflow geometry, where the continuous phase (ie. the carrier fluid) flows on both sides of the dispersed phase (ie. the fluid that is dispersed into microdroplets); and a T-junction (TJ) geometry[53], where the continuous and the dispersed phase meet at a right angle junction. In the coflow geometry, an orifice is typically added downstream of the region where the two phases meet to form a flow-focusing (FF) geometry[54] (see *Figure 2-1*).

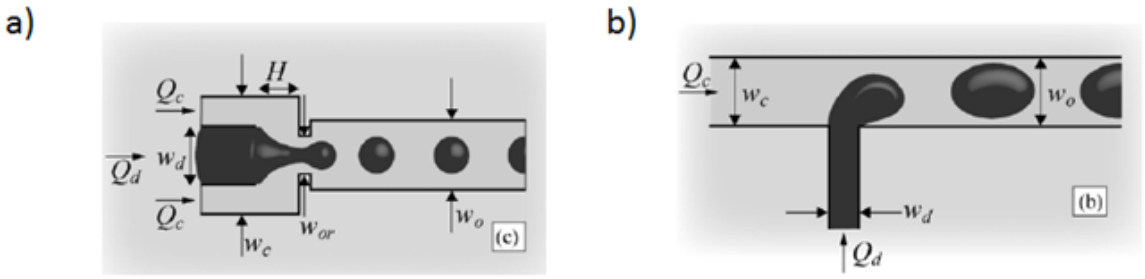

Figure 2-1 *The two main geometries used to generate microdroplets in a microfluidic device: a) flow-focusing (FF) geometry; and b) T-junction (TJ) geometry. Q_d and Q_c represent the flow rate of the dispersed and the continuous phase respectively. The relevant geometrical parameters of both devices are labeled with the letters "w" and "H".*

The main difference between the two geometries is the flow rate at which they can operate[55]. In a TJ device, the dispersed phase is pushed against the channel wall, which provides stabilization. At low flow rates, this allows a very precise control over the formation of large microdroplets. At high flow rates however, the dispersed phase does not break into droplets anymore, but rather flows continuously alongside the continuous phase. On the other hand, the FF geometry does not provide solid geometrical support to the dispersed phase, which is instead sheared from both sides by the continuous phase. As a result, the FF geometry is not stable at low flow rates but allows microdroplet generation at high flow rates. Typically, the maximal dispersed phase flow rates at which a FF device can still produce monodisperse water microdroplets is on the order of a few tens of µL/min[54,56]. The droplet diameter usually ranges from tens of µm to hundreds of µm, which yields a maximal frequency of production of ranging from 1 to 10 kHz. However, the viscosity of the dispersed phase limits the ability to operate at high flow rates.

Similarly to geometrical support, an increased viscosity stabilizes the dispersed phase and eventually prevents to formation of microdroplets. As a results, the frequency of production of polymer microcapsules is typically reduced by an order of magnitude[32].

2.2 Droplet formation mechanism

In both geometries, the dispersed phase extends out of its channel and is deformed by the viscous shear stress imposed by the continuous phase until it irreversibly collapses due to Rayleigh-Plateau instability driven by surface tension equilibration[57]. The balance between these two forces is essentially described by the dimensionless *Capillary number* (Ca) [58]:

$$(1) \quad Ca = \frac{viscous\ forces}{surface\ tension} = \frac{\mu_c v_c}{\gamma},$$

where μ_c and v_c are the dynamic viscosity and the velocity of the continuous phase, and γ is the surface tension between the two phases (note: the subscripts *c* and *d* are used to designate the continuous and the dispersed phase respectively). A quick dimensional analysis reveals that the Ca number is indeed dimensionless:

$$(2) \quad \left[\frac{\mu_c v_c}{\gamma}\right] = \frac{(Pa \cdot \cancel{s})\left(\frac{m}{\cancel{s}}\right)}{\frac{N}{m}} = \frac{\left(\frac{\cancel{N}}{m^2}\right)(m)}{\frac{\cancel{N}}{m}} = \frac{\cancel{m^2}}{\cancel{m^2}}$$

In the presence of geometrical constrictions, the obstruction caused by the dispersed phase leads to an increase in hydrostatic pressure which further contributes to the deformation of the dispersed phase[59]. At high flow rates, inertial forces become significant even at the microscale. This effect is captured by the dimensionless *Weber number* (We), which is defined as the ratio of inertial forces to interfacial tension:

$$(3) \quad We = \frac{inertial\ forces}{surface\ tension} = \frac{\rho_d d_d {v_d}^2}{\gamma},$$

where ρ_d, $d_d$and v_d are the density, diameter and velocity of the dispersed phase. Once again, a dimensional analysis reveals that the We number is dimensionless:

$$(4) \quad \left[\frac{\rho_d d_d v_d}{\gamma}\right] = \frac{\left(\frac{kg}{\cancel{m^3}}\right)(\cancel{m})\left(\frac{\cancel{m^2}}{s^2}\right)}{\frac{N}{m}} = \frac{\frac{kg \cdot m}{s^2}}{N} = \frac{\cancel{N}}{\cancel{N}}$$

At low Ca, the rate at which the dispersed phase is deformed is slow compared to surface tension relaxation. As a result, the collapse proceeds through a series of reversible equilibrium states (stage 1 of collapse) up to a point where the interface becomes unstable and pinches off due to a regular Rayleigh-Plateau instability (stage 2 of collapse). In stage 1, surface tension resists the deformation of the dispersed phase induced by viscous shear stress and hydrodynamic pressure. In stage 2 however, the dispersed phase neck is so thin that surface tension favors the microdroplet to detach. The duration of this second phase is very short compared to the first one and as a result, the microdroplet volume is almost entirely determined by a quasistatic process[59]. The microdroplets formed via this two-stage *dripping* regime are very uniform in size and typically pinch-off near the region where the two phases meet.

At high We, the dispersed phase momentum is high compared to the rate at which it is deformed. As a result, the dispersed phase does not collapse near the region where the two phases meet, but rather extends further downstream and forms a thin thread (see *Figure 2-2*). In this *jetting* regime, absolute and convective instabilities can occur[60]. In the first case, disturbances at the surface of the dispersed phase thread grow and propagate both upstream and downstream of the point where they originated. The thread surface thus oscillates (ie. capillary waves) and eventually breaks into microdroplets. In the second case, the disturbances only propagate downstream as they grow, which allows the dispersed phase to flow continuously without collapsing.

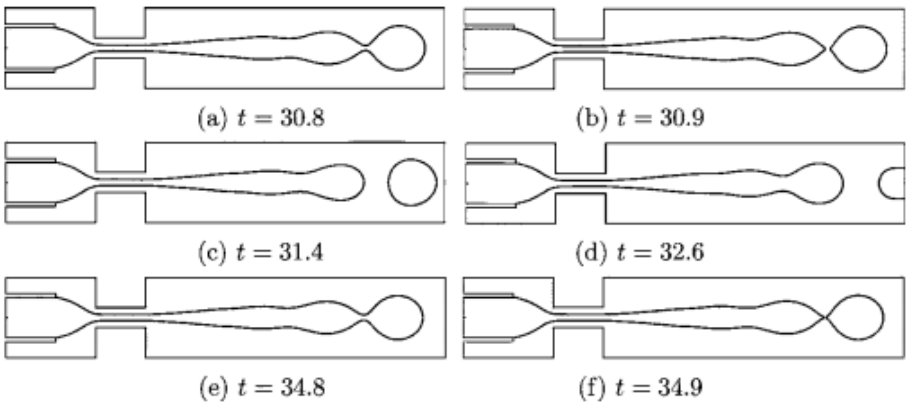

Figure 2-2 *Simulation of the absolute instabilities in the jetting regime in a FF device. At high We, the dispersed phase forms a thread which extends past the nozzle of the FF device and collapses due to capillary waves.*

In the stage 2 of the dripping regime, the dispersed phase forms a very thin neck that breaks due to capillary oscillations similar to the one described in the case of jetting. These oscillations are influenced by many factors including interaction with the channel walls, length of the dispersed phase neck, viscosity ratio of the two phases and position of the initial disturbance that triggered the oscillations[61]. The complex interplay between these factors can cause the neck to break in multiple points almost simultaneously, forming one or more small satellite droplets alongside the mother droplet. Typically, the volume of these satellite droplets is insignificant compared to the volume of the mother droplet (see *Figure 2-3*).

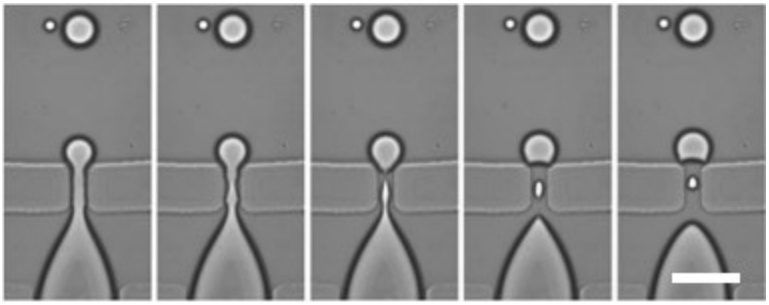

Figure 2-3 *In stage 2 of the dripping regime, the dispersed phase neck breaks due to capillary waves similarly to the jetting regime. In some cases, the neck breaks in multiple points, leading to the formation of small satellite droplets (scale bar = 160 µm).*

2.3. Microdroplet size scaling

As the dispersed phase advances in the nozzle, it fills a droplet that eventually detaches from the thread. The volume *V* of this droplet is simply the product of the dispersed phase flow rate Q_d and the time between each collapse τ. As mentioned in the previous section, the dispersed phase is deformed by the shear stress imposed by the continuous phase. An increase in the continuous phase flow rate Q_c thus increases the rate at which the dispersed phase is deformed, and leads to a proportional decrease of τ. Consequently, a simple scaling relation between the microdroplet volume and the ratio of both flow rates is obtained:

$$(5) \quad V \propto \frac{Q_d}{Q_c}.$$

This relation has been demonstrated experimentally in both the FF geometry[62] and the TJ geometry[63]. In order to predict the microdroplet volume more precisely, device geometry, fluidic

properties (such as viscosity and density) and surface tension between the two phases must be taken into account[29]. However, this analysis is quite involved and beyond the scope of this project.

2.4. Cell encapsulation

Cells suspended in the dispersed phase are naturally encapsulated as the microdroplets are formed (see Figure 2-4). Ideally, all cells would be singly encapsulated to ensure sample uniformity. However, the local cell concentration in the dispersed aqueous phase fluctuates around a known average (ie. the overall concentration at which the cells were initially suspended), which causes cell occupancy[11] to vary. The probability to encapsulate *N* cells in one microdroplet given an average cell occupancy of <*N*> cells per microdroplet is thus described by the Poisson distribution[64] :

$$(6) \quad f(N;\langle N\rangle) = \frac{N^{\langle N\rangle} e^{-N}}{\langle N\rangle!}.$$

To overcome the inefficiency of random encapsulation, inertial ordering[56] and hydrodynamic self-sorting[65] can be used.

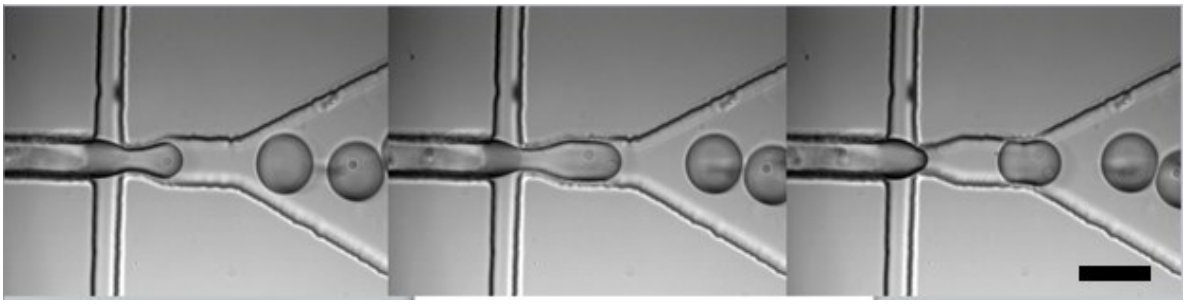

Figure 2-4 *Cell encapsulation in a FF microfluidic device: cells suspended in the dispersed phase are encapsulated as the microdroplets are formed following Poisson distribution (scale bar = 100 µm).*

2.5. Microcapsule collection

In order to completely remove the oil phase and resuspend the microcapsules in their final aqueous medium, conventional and microfluidic methods typically go through many off-chip centrifugal/rinsing cycles[19,20,47]. Since organic solvents and high centrifugal forces must be avoided to preserve cell viability, the process requires a long time, which leads to decreased cell viability[39]. Furthermore, microcapsules can be lost during the rinsing process[39] and in some cases, they aggregate upon exiting the microfluidic device[66]. To circumvent these issues, on-chip transfer of the microcapsules from their original oil carrier phase to a continuous aqueous phase has been demonstrated[39,40]. The main idea is to take advantage of the laminar flow conditions at the

[11] The number of encapsulated cells per microdroplet

microscale to generate a laminar interface between the two continuous phases. It was observed that microcapsules in the vicinity of the interface migrate to the continuous aqueous phase if it contains the fastest stream lines[40].

Chapter 3 EXPERIMENTAL SETUP AND METHODS

3.1. Microfluidic design

The geometry of the microfluidic device was designed to meet the objectives set in the introduction chapter. In order to maximise the throughput of the operation, a FF geometry was chosen over its TJ counterparts since it can operate at higher flow rates. The main components of the design elaborated are shown in *Figure 3-1*. The continuous and the dispersed phase meet upstream of the nozzle, where hydrodynamic pressure and viscous shear stress causes the collapse of the dispersed phase into microdroplets. The nozzle then leads into a larger channel intended to slow down the microdroplets to allow visualization. The dimensions of our FF geometry were inspired by the design of Edd *et Al.*[56], who successfully demonstrated high-throughput cell encapsulation in monodisperse water microdroplets.

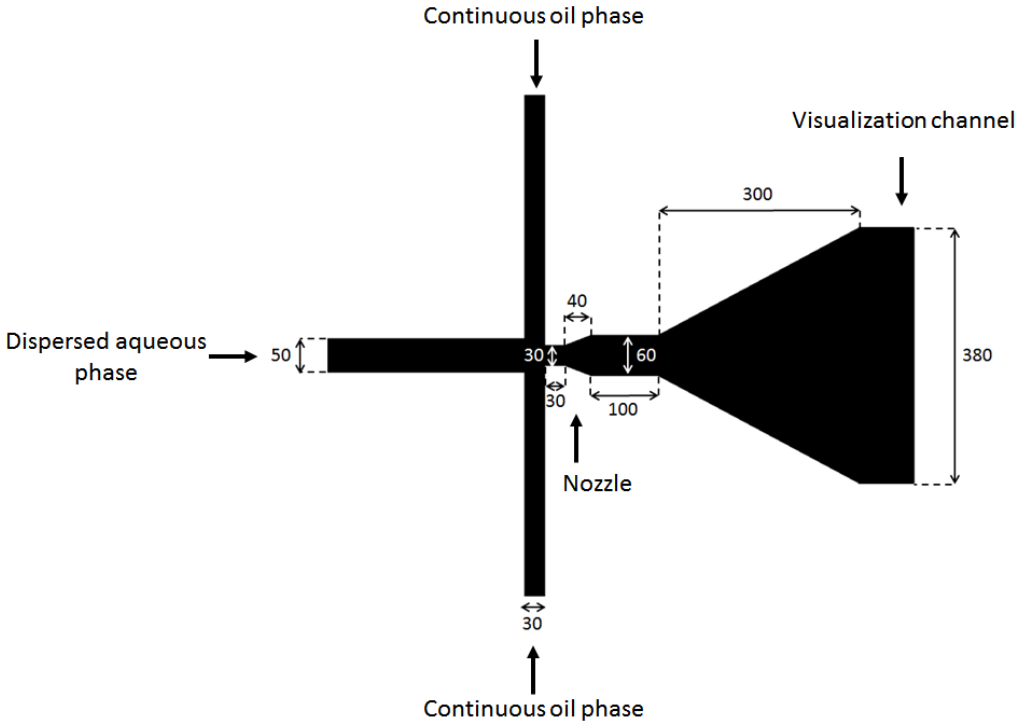

Figure 3-1 *a) The main components of the FF design: the continuous and dispersed phase meet upstream of the nozzle where the microdroplets are formed. The microdroplets are then slowed down in the wider visualization channel; and b) the exact dimensions of the design (all dimensions are in µm).*

Given the size of the cells to be encapsulated (from 15 µm to 25 µm), the initial device was designed to allow the production of microdroplets with a diameter of approximately 45 µm to ensure that a sufficiently thick layer of polymeric matrix would surround the cells. Edd *et Al.* design

featured a 16 µm nozzle and produced microcapsules with diameters ranging from 30 µm to 35 µm. Consequently, we increased the nozzle width to 30 µm with the intention of generating slightly larger microcapsules. We also increased the width of the dispersed phase and continuous phase inlets to maintain the proportionality of the design. The height of the channels was originally set to 45 µm to produce microcapsules of similar dimensions. However, it was later increased to 90 µm to allow the production of larger microdroplets. The enlargement sections downstream of the nozzles were designed to be very gradual to avoid dead volumes and we maximized the width of the visualization channel to slow down the microcapsules. A width of 380 µm was chosen to prevent the collapse of the channel.

Different designs have been investigated for the three channels leading into the FF geometry (see *Figure 3-2*). In the first design, the aqueous and the oil phase were each injected via a single access hole. The two side channels were exactly the same length to ensure that the flow of the oil would be symmetric. This design was operational, but was prone to clog if impurities entered the device. Although all solutions were thoroughly filtered through a 0.22 µm mesh, PDMS shards generated by the hole punching procedure (see *3.5.* Microfabrication) were pushed in the device when fluids were first injected.

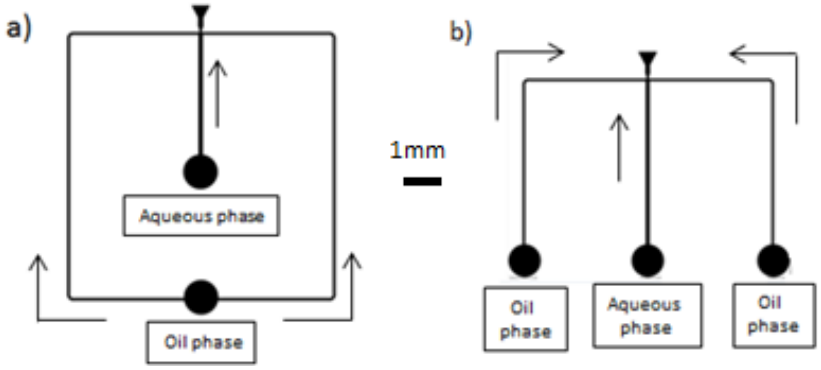

Figure 3-2 *Design of the three channels leading into the FF geometry. a) the aqueous and the oil phase are each injected via a single access hole; b) the oil phase is injected via two access holes to allow independent control of the pressures applied to the two side channels (scale bar = 1mm).*

In order to remove these debris, a second access hole was added for the oil phase, which allowed independent control of the pressure applied to the two side channels. Consequently, if one of the side channels was obstructed, the flow could be reversed to push back the shards through the access hole. A long asymmetric serpentine geometry was also considered for the dispersed channel. Edd *et al.*[56] have shown that at high flow rates, this geometry causes the cells to self-organize into evenly spaced streams. By tuning the microdroplet formation accordingly, they could reduce the

number of unoccupied microcapsules significantly[56]. However, this method seemed quite complex to execute since it required a precise optimization of flow rates, channel geometry and droplet formation frequency. Consequently, we decided to rely on random encapsulation.

In order to obtain on-chip gelation of the agarose microcapsules, a serpentine channel was added downstream of the FF geometry and a temperature gradient was established across the microfluidic device (see *Figure 3-3*). For this purpose, an external temperature control system was designed and machined (see *3.2. Temperature control* system). Using this system, the temperature of the FF geometry and the serpentine channel could be controlled independently. In general, the temperature of the FF geometry was set to ~37°C to prevent gelation of the agarose solution before the microdroplets were formed and to maintain cell viability. On the other hand, the temperature of the serpentine was lowered to its minimal value (~6°C) to optimize the gelation process. The length of the serpentine channel was set to 144 mm. Since the microdroplet typically traveled at speeds ranging from 1 to 15 mm/s, this allowed more than 2 minutes of on-chip gelation time.

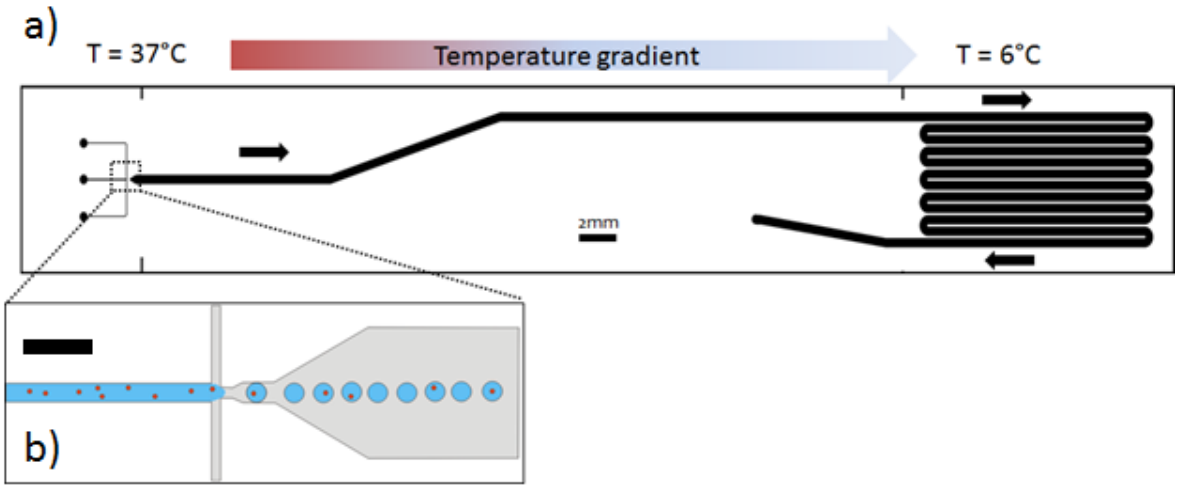

Figure 3-3 a) *Microfluidic design including a FF geometry maintained at 37°C for cell encapsulation and a serpentine channel maintained at 6°C for microcapsule gelation (scale bar = 2 mm); b) close-up view of the FF geometry illustrating the encapsulation process (scale bar = 100 µm).*

The two-module microfluidic design presented above was used for most of the experiments presented in this thesis. It was found to allow high-throughput generation of monodisperse microcapsules (see Chapter 4), continuous on-chip gelation (see Chapter 5), and controlled cell encapsulation with maintained viability (see Chapter 6). To demonstrate that the proposed system is also compatible with on-chip downstream processing, a third module allowing the microcapsule purification was added. The purpose of this module is to transfer the gelled microcapsules from

their original oil carrier fluid to an aqueous carrier fluid, while extracting the oil in the same process. The first design was inspired by Deng *et al.*[39]. It featured a set of perpendicular side channels on both sides of the main channel containing the microcapsules carried in the oil phase. An aqueous solution is injected on one side, compressing the oil phase and forcing it out the opposite side, creating a laminar interface between the two fluids (see *Figure 3-4*a). However, instead of migrating towards the continuous aqueous phase, the microcapsules remained in the oil phase and squeezed through the small channels intended for oil removal (see *Figure 3-4*b).

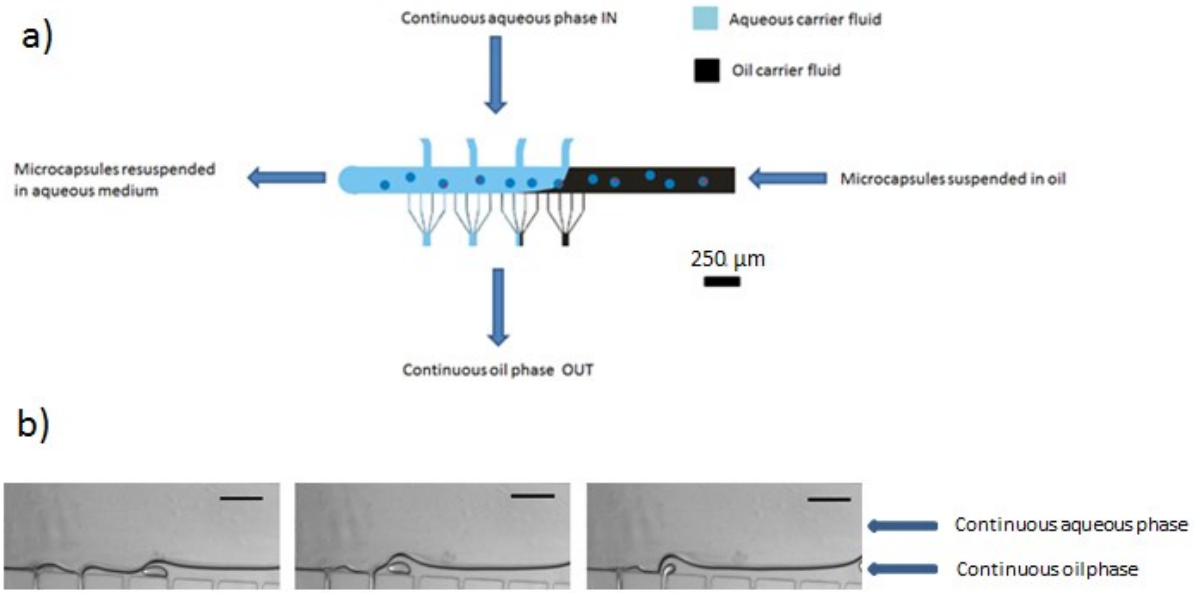

Figure 3-4 a) *Design for the on-chip purification of the microcapsules: a continuous aqueous phase is injected via a set of channels located on one side of the main channel, which forces the continuous oil phase to exit the device via a second set of channels located the opposite set of channels (scale bar = 250 µm).* ***b)*** *Close-up view of a water microdroplet in the vicinity of the oil-aqueous interface. Instead of migrating towards the aqueous phase, the microdroplet remains in the oil phases exits the device via a side channel intended for oil removal (scale bar = 100 µm).*

Consequently, a second design was developed to prevent the loss of microcapsules. In this design inspired by Wong *et al.*[40], the continuous aqueous solution is injected from a single side channel, and forced to flow alongside the continuous oil phase in a narrow channel leading to a bifurcation. Because of the high flow rate of the injected aqueous phase, the oil phase is compressed against the side wall of the narrow channel, forming a thin thread (see *Figure 3-5*). This design was found to allow the on-chip phase transfer of the microcapsules while extracting the oil phase, and will be discussed in details in Chapter 7.

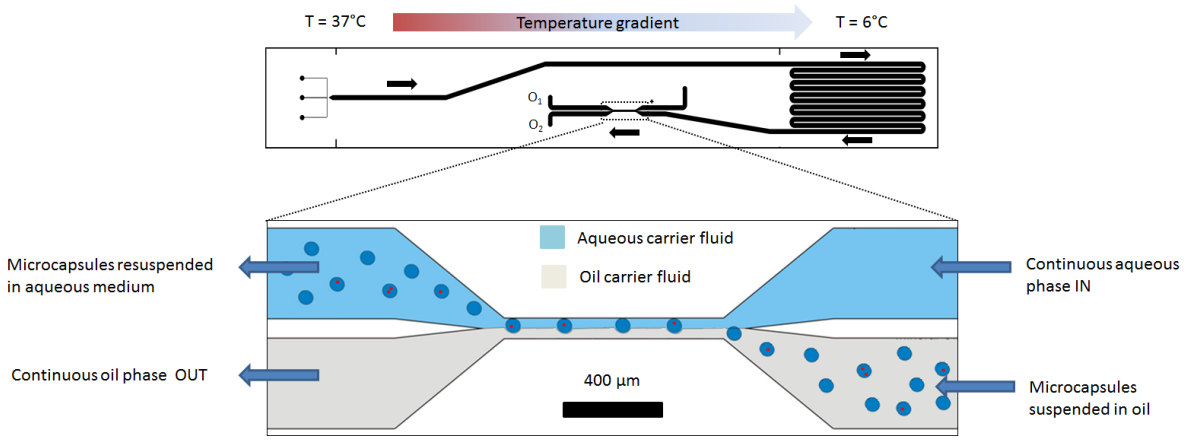

Figure 3-5 *a) Design of the three-module microfluidic device for cell encapsulation, microcapsule gelation and purification; b) close-up view of the microcapsule purification module. A continuous aqueous phase is injected via a side channel and flows alongside the continuous oil phase in a narrow channel. The compression of the oil phase causes the microcapsules to migrate towards the aqueous phase. The oil is then removed via a downstream bifurcation (scale bar = 400 µm).*

3.2. Temperature control system

As stated in the previous section, microcapsule gelation was achieved by establishing a temperature gradient across the microfluidic device. For this purpose, a temperature control system was designed and machined. It comprises three components: a heat sink, a heating block and a cooling block (see *Figure 3-6*). Aluminum was chosen because of its relatively high specific heat capacity, providing the system with an adequate thermal mass to minimize temperature fluctuations. A first thermoelectric (TE) module[12] (HP-127-1.0-1.3-71, TEtech) is placed between the heating block and the heat sink, pumping heat from the heat sink to increase the temperature of the heating block. A second TE module is placed between the cooling block and the heat sink, pumping heat from the cooling block to decrease its temperature. Thermal compound (MX-4, Arctic) is applied on both sides of the TE modules to maximize heat transfer. The heat sink dissipates excess heat generated by the TE modules through circulating water maintained at 37°C. The microfluidic device is inserted in the temperature control system from the bottom and two aluminum plates are used to secure the device in place and maximize heat transfer. An opening was made in the heating plate to allow visualization of FF geometry, which was found to be crucial for the initial stabilization phase of the encapsulation process. Furthermore, two small holes were machined on each side of the heatsink to maintain the sample and collection vials at 37°C during the procedure.

[12] TE modules are solid-state heat pumps operating on the Peltier effect. Briefly, when a voltage is applied across the semi-conductor array, the movement of charge carriers causes heat to be absorbed on one side of the module and rejected on the other side. This effect can be reversed by simply inverting the flow of the current through the module.

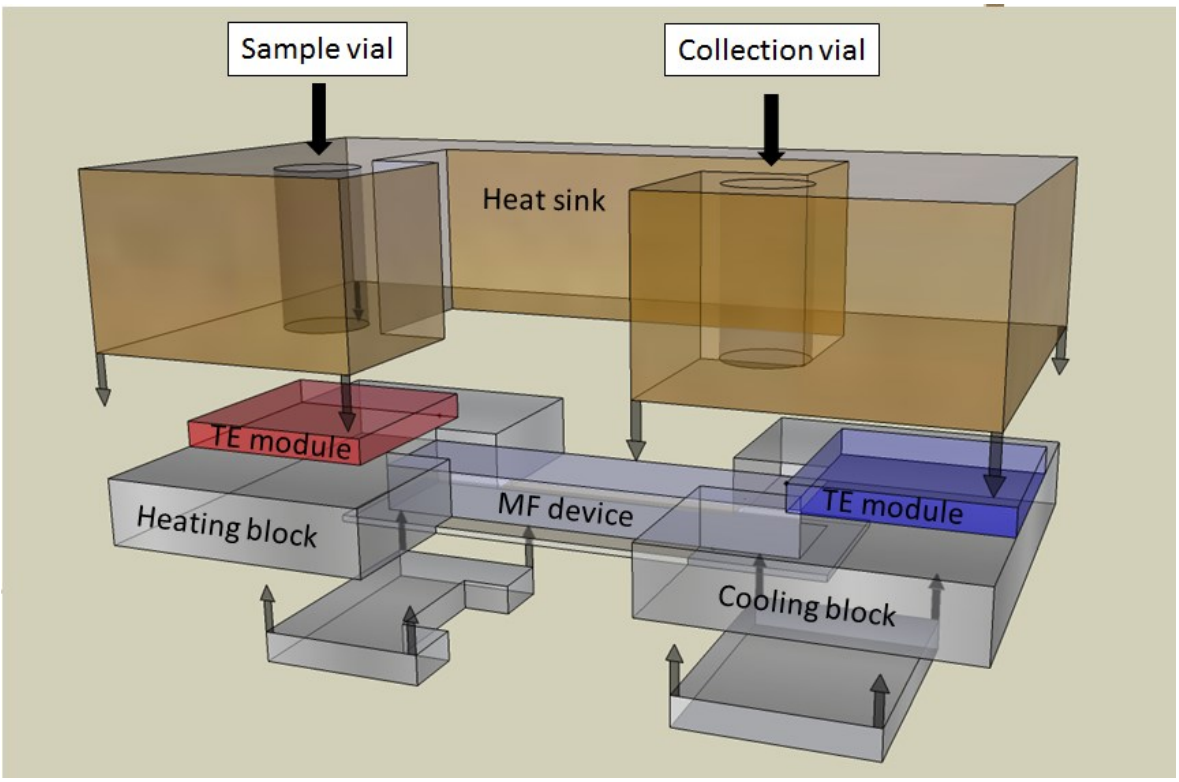

Figure 3-6 *Exploded view of the temperature control system used to generate a temperature gradient in the microfluidic device. A heating block is used to maintain the FF geometry at 37°C and a cooling block is used to maintain the serpentine channel at 6°C. A heat sink dissipates excess heat generated by the TE modules.*

To ensure that the TE modules pumped the adequate amount of heat, each of them is connected in a feedback loop with a thermistor (MP-2444, TEtech) via a temperature control chip (HTC 3000, Wavelength Electronics). A LabVIEW program is used to input the target temperature, which is converted to a voltage and sent to the temperature control chip as a setpoint via a data acquisition (DAQ) module (NI USB-6212, National Instruments). The thermistor is fed a sensor bias current of 100μA and the current through the TE module is automatically adjusted by the control chip until the voltage across the thermistor equals the setpoint voltage.

To confirm the functionality of the temperature control system, a microfluidic device punctured with access holes was inserted. The heating and cooling block temperatures were set to 45°C and 0°C respectively. The temperature of both blocks was measured as a function of time (see *Figure 3-7*). It was found that the heating block stabilized at around 44°C after about 1 minute, while the cooling block stabilized at around -1°C after about 10 minutes. The temperature of the heatsink directly above both blocks did not vary significantly during the process, which means that excess

heat produced by the TE modules was efficiently removed, allowing long-term operation of the system.

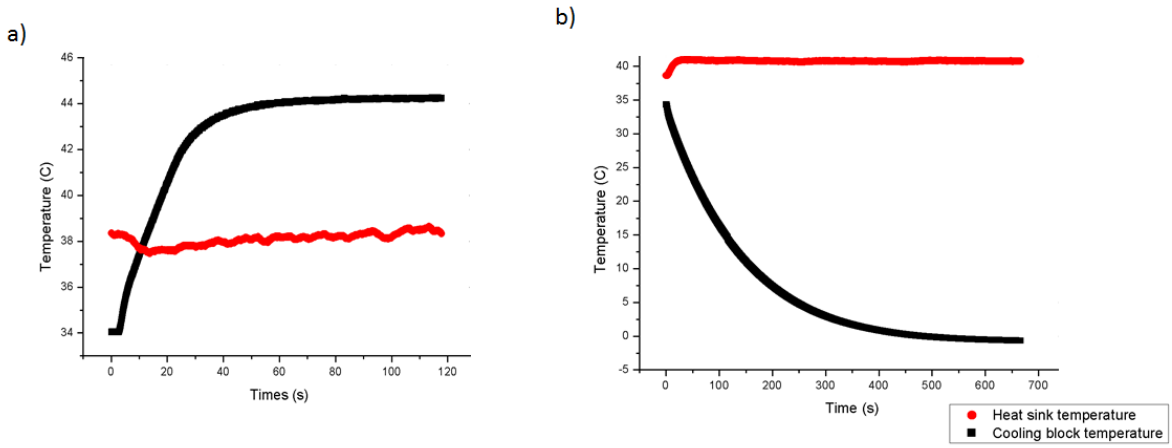

Figure 3-7 *Temperature as a function of time for a) the heating block and the region of the heatsink directly above it; b) the cooling block and the region of the heatsink directly above it. Both blocks stabilize near the set temperatures, while the heat sink temperature does not vary significantly.*

The temperature of the microfluidic device was probed by inserting a thermistor in access holes along the main channel. Measurements were taken from the dispersed aqueous phase inlet to the end of the first segment of the serpentine channel. It was found that the temperature of the FF geometry ranged from 36°C to 35°C while the temperature of the serpentine ranged from 8°C to 6°C (see Figure 3-8). The temperature gradient across the device was almost linear, presenting a flatter region in the middle of the device. This is due to heat loss, which caused the middle of the region to remain at room temperature.

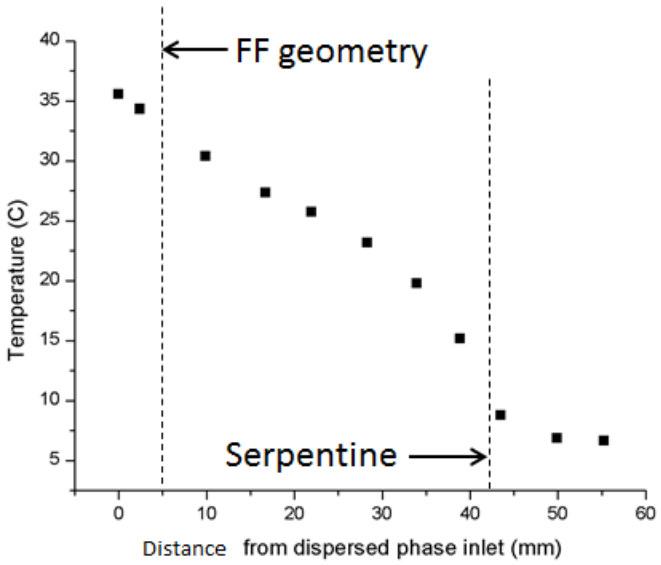

Figure 3-8 *a) Temperature of the microfluidic device as a function of distance from the dispersed phase inlet. The FF geometry (from 0 to 5 mm) was maintained between 35 and 36°C while the serpentine (from 42 to 55 mm) was maintained between 6 and 8°C (the error bars are contained within the symbols).*

3.3. Pneumatics

A pneumatic system is used to provide the pressure which drives the fluids into the microfluidic device (see *Figure 3-9*).

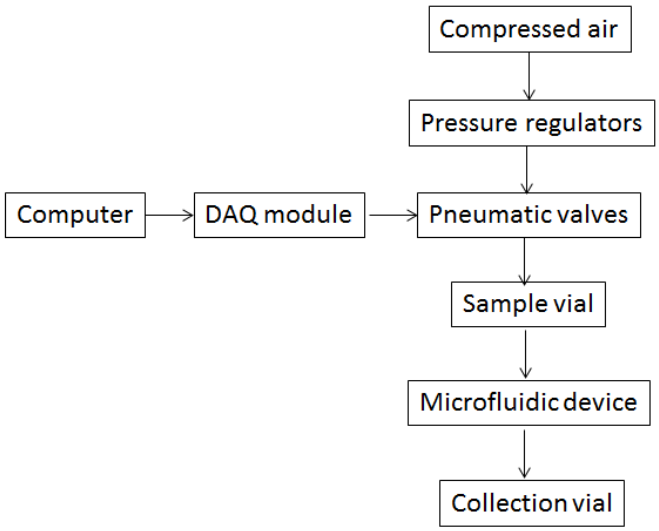

Figure 3-9 *Schematic of the pneumatic system used to control the fluids in a microfluidic system.*

Compressed air is fed to pressure regulators (IR2010-N02-R, SMC Pneumatics), which are used to precisely control the pressure applied to the fluids. Pneumatic valves (S070 C6DG 32, SMC

Pneumatics) actuated by a 12 V DC voltage allow the user to turn the pressures ON and OFF via a LabVIEW program. The air flowing out of the pressure regulators pressurizes sealed vials containing the samples. The vials are connected to the microfluidic device via microfluidic tubing.

3.4. Image acquisition

The cell encapsulation setup is mounted on an inverted microscope (Olympus IX-51), interfaced with a CCD camera (GC Prosilica, Allied Vision Technologies). The camera exposure time, region of interest (ROI) and frame rate can be controlled via a LabVIEW program. The ROI and the exposure time were reduced to optimize the frame rate, which typically varied from 50 to 300 fps. To overcome the camera frame rate limit, repetitive events (such as the production of microdroplets) were imaged using a stroboscopic effect (ie. the frame rate was adjusted to be slightly slower than the frequency of droplet production). This allowed the clear visualization of the details for very fast processes (see *Figure 4-2* and *Figure 4-5*). The size-to-pixel calibration constant of the camera was measured for different magnifications. To do so, a photomask with well-defined features of known dimensions was photographed and the number of pixels constituting the features was counted using ImageJ. Bright field microscopy is typically used to visualize microcapsules suspended in oil, but phase contrast microscopy is required to clearly distinguish microcapsules suspended in an aqueous solution (see *Figure 3-10*).

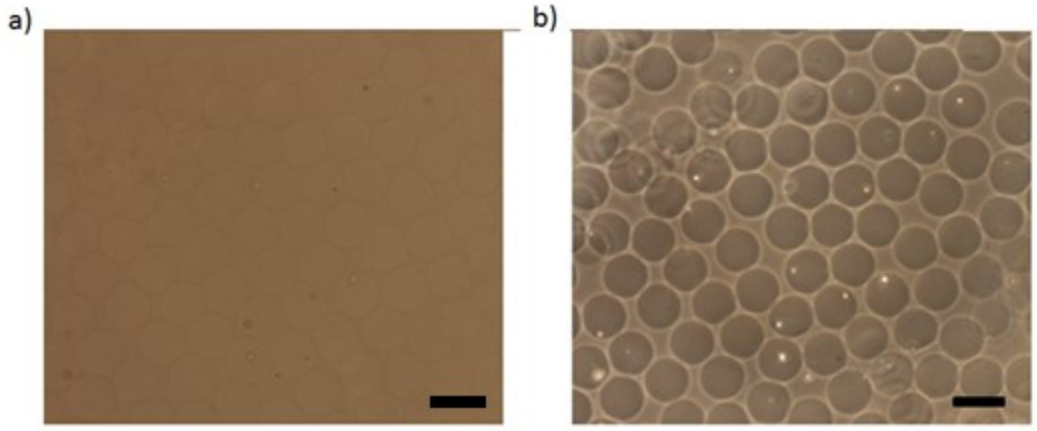

Figure 3-10 *Agarose microcapsules suspended in phosphate buffered saline (PBS) visualized with a) BF microscopy (scale bar = 60 µm) and b) phase contrast microscopy. The white dots are traces of oil in the sample (scale bar = 60 µm).*

An epi-fluorescence microscope (Nikon Eclipse TiE) was used to assess the viability of the encapsulated cells following different procedures; an A1R laser scanning confocal microscope was used to clearly visualize the position of a cell within a microcapsule.

3.5. Microfabrication

(see Appendix I for more details about the procedure)

Soft lithography[67] is used for the microfabrication of the microfluidic devices. Firstly, the network of microchannels is designed in a CAD program (CleWin4), and subsequently imprinted on a negative polarity photomask (CAD/Art Services) using a high-resolution printer. A piranha etch is then performed on a silicon wafer (University wafer) to remove all organic residues and hydroxylate the surface, making it highly hydrophilic. A thin layer of SU-8[13] (Microchem) is spun-coated onto the clean dehydrated wafer (Laurell Spin Coater, model WS-400BZ-6NPP-LITE). The spin speed is adjusted based on the photoresist viscosity and the desired film thickness, which later dictates the height of the microfluidic channels. The photoresist is soft baked to evaporate the solvent and densify the film, and the wafer is then placed in vacuum contact with the transparency to selectively expose the film to near UV light (OAI DUV/NUV mask aligner, model 206). The exposure time is adjusted based on the film thickness in order to obtain optimal cross-linking. A post-exposure bake is then used to promote cross-linking of the exposed regions of the film after which the wafer is immersed in SU-8 developer (Microchem) to remove all uncross-linked photoresist. Finally, the wafer is coated with chlorosilane to decrease its surface energy and preserve its features. The wafer, with the microchannel network embedded as a *bas-relief* on the surface is then ready to serve as a master for replica molding. A stylus profiler (Veeco/Sloan Dektak 3 30) is used to confirm the height of its features. Using this technique, master molds with 45 µm and 90 µm height features were fabricated (see *Table 1* for the detailed parameter used).

Feature height	45 µm	90 µm
SU-8 type	SU-8 2050	Su-8 2075
Spin speed (rpm)	3000	3000
Soft bake time (min)	1@65°C and 6@95°C	5@65°C and 10@95°C
Exposure time (s)	11	15
Post-exposure bake time (min)	1@65°C and 6@95°C	2@65°C and 8@95°C
Developing time (min)	4	8

Table 1 *Microfabrication parameters used to obtain different master mold feature heights.*

Polydimethylsiloxane (PDMS) is an excellent elastomer material for the fabrication of microfluidic devices for use with biological material[68]. Its main advantages include: the ability to reproduce the micron-sized feature of the master mold accurately; transparency to visible and short wave UV light; biocompatibility and permeability to O_2 and CO_2; elasticity; controllable surface

[13] An epoxy-based negative photoresist that polymerizes upon near UV (350-400nm) exposure

chemistry; the ability to seal irreversibly to different materials (including itself and glass) to form closed microchannels; and the non-damaging release from the master mold. To form PDMS, a curing and a base agent (Sylgard 184 elastomer kit) are mixed in the ratio of 10 to 1 to obtain the desired PDMS elasticity. The PDMS is then degassed, casted on the master mold and heated to accelerate the reaction. Once cured, the PDMS is peeled-off and cut into separate microfluidic devices, access holes are punched and the devices are cleaned. The PDMS devices and glass slides are oxidized using an O_2 plasma discharge (Glowresearch Autoglow Oxygen Plasma System), and immediately placed against each other to form an irreversible seal (see *Figure 3-11*). The plasma oxidization has the additional effect of replacing PDMS surface methyl groups (Si-CH_3) by silanol groups (Si-OH), rendering the PDMS surface hydrophilic and easily wettable by aqueous solutions[69]. However, the PDMS surface recovers its native hydrophobicity with time due to the migration of low molecular weight oligomers from the bulk of the PDMS to the surface[70].

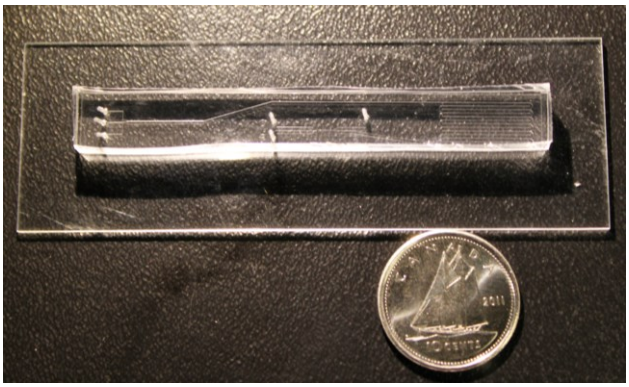

Figure 3-11 *Photograph of the three-module microfluidic device produced by replica molding.*

3.6. Reagents

The main concerns for the choice of reagents were compatibility with the encapsulated cells and with the microfluidic device. In conventional cell encapsulation methods, mineral oil and silicone oil are typically used as the continuous phase because of their ability to preserve cell viability. However, since the proposed microfluidic device are made of Polydimethylsiloxane (PDMS), silicone oil could not be used because it would swell the device significantly[71]. Fluorocarbon oils were considered because of their increased gas permeability and their ability to reduce the leaking of the biological material out of the microcapsules [72]. However, the range of surfactants compatible with these oils is very limited[73]. Consequently, it was decided to use light

mineral oil (Sigma-Aldrich). The compatibility of mineral oil with PDMS was confirmed by simply filling a microfluidic device with oil and observing its features. No swelling was observed.

To prevent coalescence of the microdroplets prior to their gelation, surfactants[14] are typically used. Because of their amphiphilic nature, surfactants adsorb at oil-aqueous interface and stabilize the emulsions by reducing surface tension. Based on the relative strength of their polar and non-polar groups, surfactant either favors the formation of aqueous microdroplets in oil or oil microdroplets in water [74]. The most commonly used surfactant soluble in mineral oil and promoting the formation of aqueous microdroplets is SPAN 80 (ie. Sorbitan monooleate)[73]. Since SPAN 80 also showed good biocompatibility for the encapsulation of yeast cells[75] and mouse embryonic stem cells[48], we chose to use it for our application.

3.7. Cell culture

(see Appendix I for more details about the procedure)

3T3 cells – an immortalized fibroblast mouse cell line – were chosen as a cell model for encapsulation because of their robustness, availability and low biohazard risk. Cells are cultured in Dulbecco's Modified Eagle Medium (DMEM) (high-glucose, including 10% fetal bovine serum and 1% penicillin-streptomycin) (Hyclone) in a plastic petri dish, and passaged every three days with a seeding density of 1.25×10^5 cells. The cell splitting procedure includes trypsinization to detach the cells from the dish and resuspension in an agarose solution for the encapsulation process. Typically, a solution of 2% (m/V) ultra-low gelling agarose (Sigma-Aldrich) and 20% (V/V) Optiprep (Sigma-Aldrich) in Dulbecco's phosphate buffered saline (DPBS) (no Ca^{2+}/Mg^{2+}) (Multicell) is used. Prior to the resuspension in the agarose solution, a hemocytometer is used to assess the cell concentration, which is obtained by averaging the number of cells counted in each of the 4 quadrants. The volume of the cell suspension is then adjusted to obtain the desired cell concentration for the encapsulation procedure. Following the resuspension, the cells are gently vortexed to ensure a homogeneous concentration and quickly brought to the encapsulation system to prevent the agarose solution from gelling.

[14] Surface active agents comprised of a hydrophilic (polar) head group and a hydrophobic (non-polar) tail group

Chapter 4 HIGH-THROUGHPUT GENERATION OF MONODISPERSE AGAROSE MICRODROPLETS

4.1. Preliminary experiments

The device's ability to produce monodisperse droplets was first assessed using mineral oil as the continuous oil phase and deionized (DI) water as the dispersed aqueous phase at room temperature. In order to generate aqueous microdroplets reliably, it was found that the oil phase has to wet completely the microchannel walls. Inversely, if the aqueous phase wets completely the channels, oil microdroplets are formed, whereas partial wetting of the dispersed phase leads to structureless patterns randomly breaking in different regions. To obtain complete wetting of the oil phase, two strategies were combined: 1) following plasma treatment, the PDMS devices were given 48 hours to recover their hydrophobicity before they were used; and 2) a concentration of at least 1% (m/m) of SPAN 80 was dissolved in the mineral oil to increase its affinity for the dispersed aqueous phase (see *Figure 4-1*).

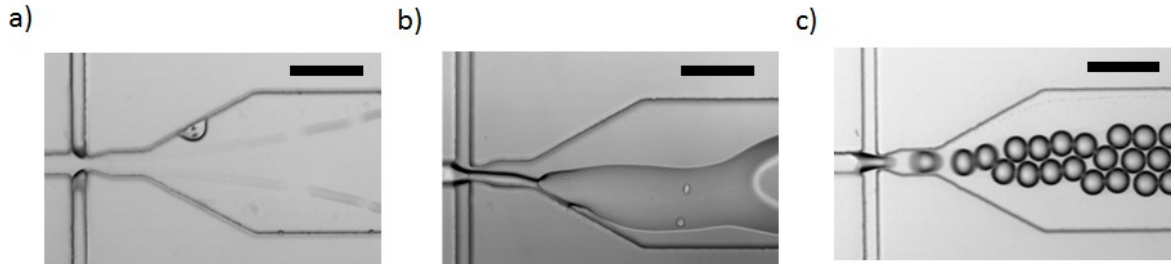

Figure 4-1 *Microdroplet formation for different PDMS surface chemistries: a) immediately after plasma treatment, the aqueous phase completely wets the channel walls even if a concentration of 1% SPAN 80 is used; b) without surfactant, the aqueous phase partially wets the channel walls even if the microfluidic device is given 48 hours to recover its hydrophobicity; and c) 48 hours of hydrophobic recovery combined with a concentration of 1% SPAN 80 allows the stable production of agarose microdroplets (all scale bars = 200 µm).*

Once stable production of microdroplets had been established, the different regimes of formation were investigated. Different values of aqueous phase pressure P_d and oil phase pressure P_c ranging from 0.040 MPa to 0.300 MPa were tested (note: the values of the applied pressures were always measured from the analog pressure regulator gauge with an estimated reading precision of ±0.005 MPa). At pressures lower than 0.040 MPa, the resistance of the device was too significant compared to P_d and P_c and the aqueous phase flowed in the oil phase side channels or vice-versa. On the other hand, pressures higher than 0.300 MPa caused frequent leaks at the interface between the tubing and the microfluidic device. Within these limits, a pressure ratio

$\Gamma = {}^{P_d}/_{P_c}$ between 0.55 and 0.75 yielded a regime very similar to the two-stage dripping regime described in Chapter 2 (see *Chapter 4 - Sections 2 and 3*). In this regime, the aqueous phase progresses through the nozzle, until it stops advancing and starts to form a neck. The neck then becomes gradually thinner until it eventually collapses to form a microdroplet (see *Figure 4-2*).

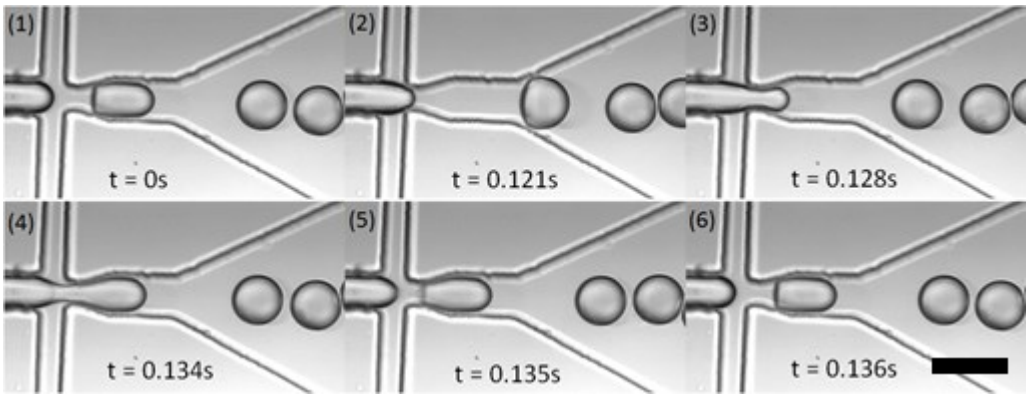

Figure 4-2 *Monodisperse formation of water microdroplets via dripping regime as a function of time (scale bar = 100 µm).*

The microdroplets produced via the dripping regime were found to be highly monodisperse. In fact, no noticeable differences could be observed and it was concluded that the variance of the microdroplet diameters was beyond the resolution limit of our experimental setup (see *Figure 4-3*). Consequently, we fixed the upper value of the uncertainty related to the measurement of the microdroplet diameters by measuring the width of the halo surrounding the boundaries of the microdroplets. The average width of the halo was 2 µm. Unless stated otherwise, the uncertainty value of ± 2 µm applies to all microdroplet diameter measurement, and is not explicitly mentioned in the text.

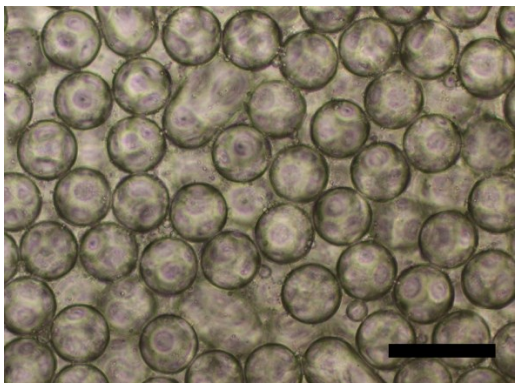

Figure 4-3 *Microdroplets produced via the dripping regime. The variance of the microdroplet diameters is beyond the resolution limit of our experimental setup (scale bar = 120 µm).*

For larger values of values the pressure ratio Γ, a regime very similar to the jetting mechanism described in Chapter 2 was also observed. In this regime, the aqueous phase extends far beyond the nozzle and forms a thin thread. Perturbations at the interface are then amplified, taking the form of capillary waves with distinct nodes. The jetting mechanism was found to produce significantly polydisperse microdroplets since the capillary waves caused the aqueous phase thread to break in different locations (see *Figure 4-4*).

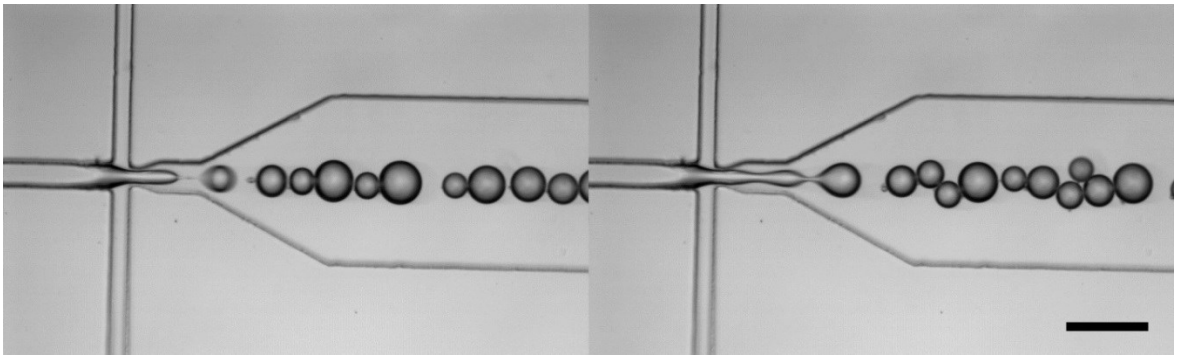

Figure 4-4 *Formation of water microdroplets via jetting regime. The capillary waves cause the aqueous thread to break in different regions, leading to polydisperse droplets (scale bar = 200 µm).*

The formation of satellite droplets was also observed, as reported by Anna *et al*.[54] (see *Figure 2-3*). As the neck of the aqueous phase becomes thinner, it eventually reaches a point where it resembles a miniature version of the jet described above. Just like in the jetting regime, capillary oscillations take place in the thin thread and cause it to break in different regions. In the dripping regime however, the volume of the thin thread is insignificant compared to the volume of the bulb at the end of the thread (see *Figure 4-5*).

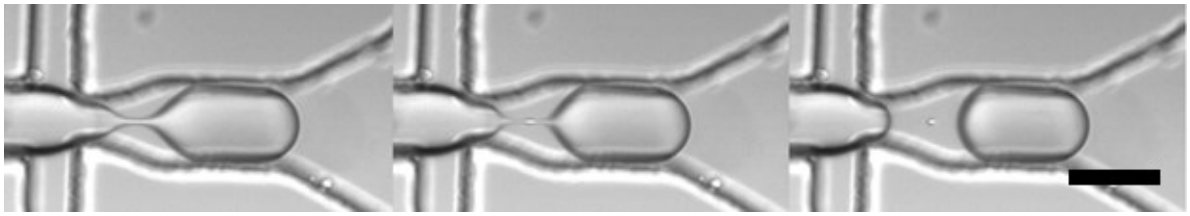

Figure 4-5 *Satellite formation in the dripping regime. The aqueous phase forms a thin neck that collapses in different regions due to capillary waves (scale bar = 60 µm).*

To confirm that the presence of satellite droplets would not impair the size monodispersity of the sample, the volume of the satellite droplet was measured for increasing values of Γ. The diameter of the satellites was found to be constant at 8 µm. This was expected since their formation is essentially driven by surface tension which stays constant. On the other hand, the main droplet

diameter increased from 21 µm to 48 µm. The ratio of the satellite droplet volume and the mother droplet volume was calculated for different values of the main droplet diameter (see *Figure 4-6*). It was found that for mother droplets larger than 25 µm, the volume ratio was less than 5%.

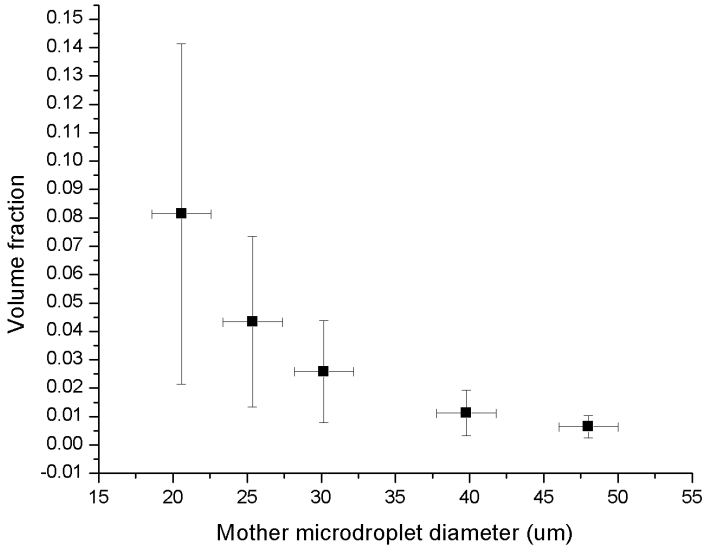

Figure 4-6 *The ratio of the volume of the satellite droplets and the mother droplets for increasing mother droplet diameter. For mother droplets larger than 25 µm, the volume ratio is less than 5%.*

4.2. Formation of agarose microcapsules

Secondly, the formation of agarose microcapsules was undertaken. Appropriate measures were taken to avoid agarose pre-gelation as much as possible. The nozzle temperature was maintained at 37°C and the serpentine region temperature at 6°C. Nevertheless, aqueous solutions with an agarose concentration of 4% and 5% contained massive patches of more viscous fluid suggesting that the gelation mechanism was already under way. These patches disrupted microdroplet formation significantly (see *Figure 4-7*) and eventually clogged the inlet tubing completely. In order to work at such agarose concentrations, the aqueous phase inlet tubing must necessarily be maintained at 37°C. However, this was not implemented on the setup because higher agarose concentrations were found to limit the throughput of the device (see *Figure 4-9*).

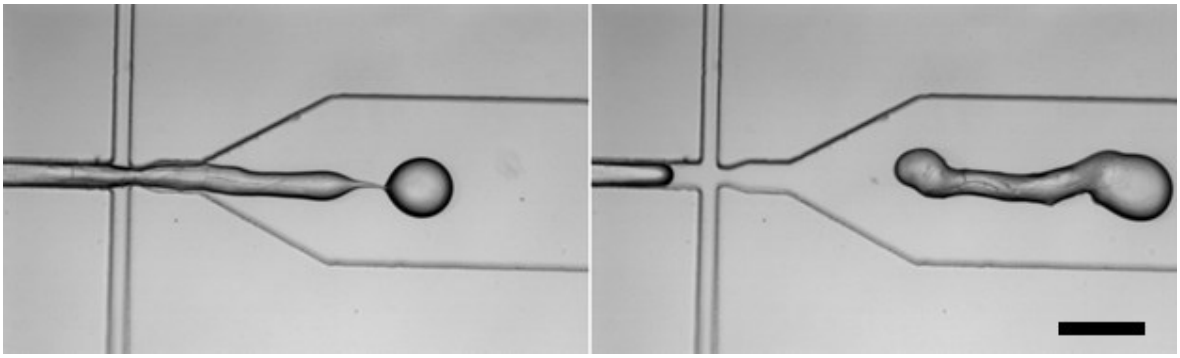

Figure 4-7 *Agarose solutions with concentration of 4% and 5% begin to gel before the microdroplets are formed, generating patches of more viscous fluid disrupting the droplet formation process (scale bar = 200 µm).*

Solutions of agarose concentration lower than 3% were not observed to contain patches of more viscous fluid. Similarly to DI water, they allowed the stable production of highly monodisperse droplets via the dripping regime (see *Figure 4-8*).

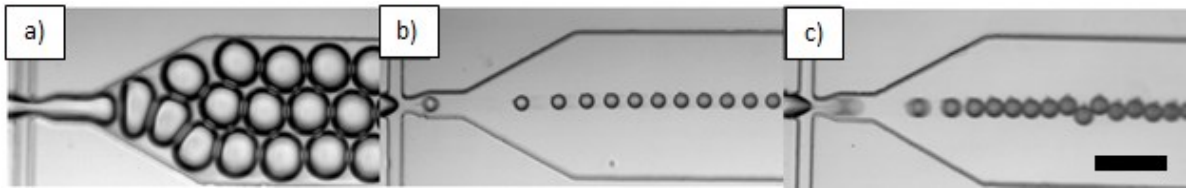

Figure 4-8 *Monodisperse formation of microdroplets via dripping regime at agarose concentration of 1% (a), 2% (b) and 3% (c) (scale bar = 200 µm).*

In order to assess the range of operation of the device, the transition from dripping to jetting was characterized as a function of P_d and P_c for values of agarose concentrations ranging from 0% to 3% (see Figure 4-9). As expected, it was found that the pressure ratio $\Gamma = {}^{P_d}/_{P_c}$ plays an important role in the droplet formation mechanism. At a critical value $\Gamma = \Gamma_{min}$, the dispersed phase and the continuous phase pressure are equal in the vicinity of the nozzle. When $\Gamma < \Gamma_{min}$, the dispersed phase is not sufficiently pressurized and is forced to backflow by the continuous phase. When $\Gamma > \Gamma_{min}$, the dispersed phase extends in the nozzle and forms monodisperse microdroplets via the dripping mechanism. At a second critical value $\Gamma = \Gamma_{max}$ however, the high momentum of the dispersed phase causes a transition to jetting. The value of Γ_{max} was found to decrease as P_c increases. At higher values of P_c, both the inertial and viscous forces increase (higher Ca and We numbers), while surface tension stays constant. Consequently, surface tension's resistance against deformation plays a decreasingly important role and jetting occurs at lower values of Γ.

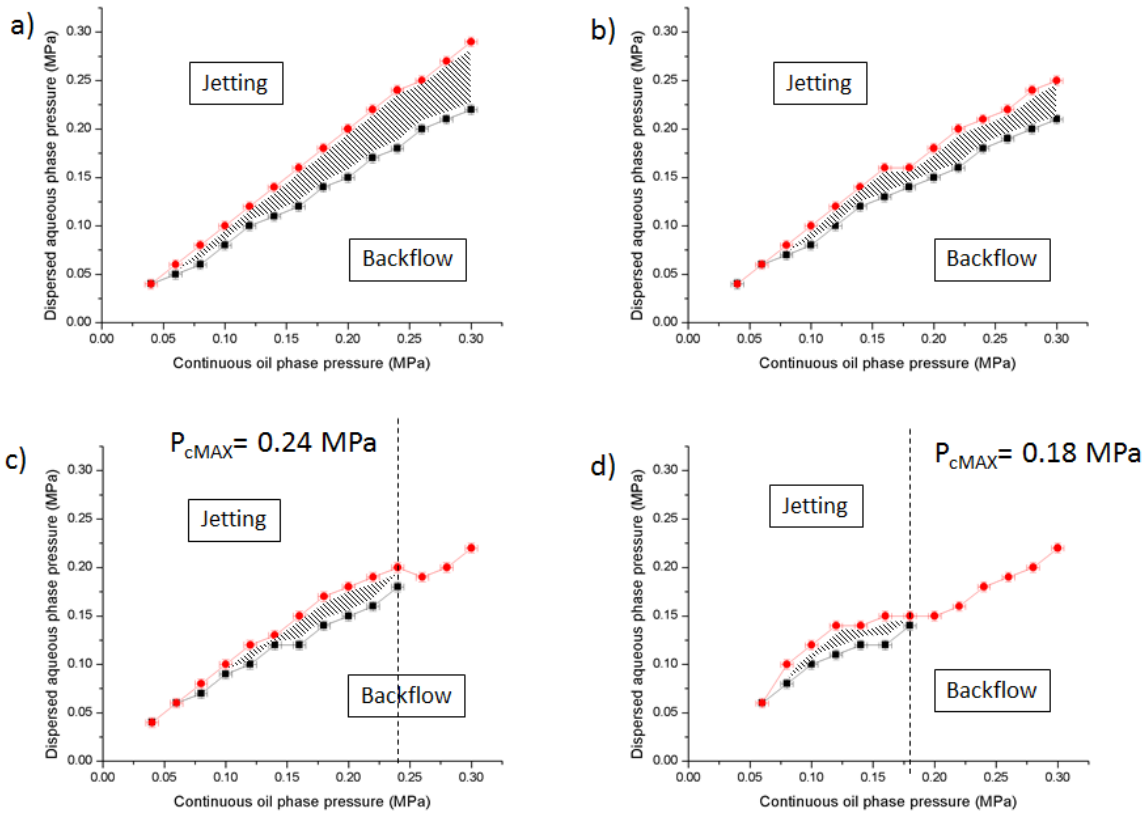

Figure 4-9 *Phase diagrams illustrating the droplet production regimes for a) DI water; b) 1% agarose in DI water; c) 2% agarose in DI water; and d) 3% agarose in DI water. The lower (black) line indicates the transition from backflow dripping, and the upper (red) line indicates the transition from dripping to jetting. The hatched region represents the range of pressures for which the dripping regime is obtained (the error bars are contained within the symbols).*

It was also observed that higher viscosities of the dispersed phase μ_d (corresponding to higher agarose concentrations) favor jetting. The reason is that μ_d opposes the deformation of the dispersed phase, which is more stable against capillary instabilities and thus more prone to extend past the nozzle and form a jet. At low μ_d (agarose concentration $\leq 1\%$), dripping can be obtained for all values of P_c tested. However, for more viscous solutions (agarose concentration $\geq 2\%$), there is a maximal value $P_c = P_{c_{max}}$ beyond which dripping cannot be obtained anymore. Instead, backflow transitions directly into jetting. We found that $P_{c_{max}} = 0.240\ MPa$ for a solution of 2% agarose and $P_{c_{max}} = 0.180\ MPa$ a solution of 3% agarose. This fundamentally limits the throughput at which droplets can be produced for a given agarose concentration. In an effort to maximise the operating range of the device while still producing mechanically strong capsules, an agarose concentration of 2% was chosen for further experiments.

4.3. Microdroplet size

As mentioned in Section 2.3, the microdroplet volume varies linearly with the ratio of the dispersed phase and the continuous phase flow rates. However, since our experimental setup was based on the use of pressure regulators, we did not have access to any direct measurements of the flow rates. Consequently, we characterized the microdroplet size as a function of the parameters we controlled, which were P_d and P_c.

The droplet diameter *a* was measured on-chip for increasing values of P_d, while P_c was kept constant. The experiment was repeated for values of P_c ranging from 0.140 MPa to 0.240 MPa. The measured values of *a* were expressed as a function of the pressure ratio Γ. All data sets were found to collapse on the same master curve and suggest the relation $a \propto \frac{P_d}{P_c}$, independently of the absolute values of P_d and P_c (see *Figure 4-10*a). This implies that the microdroplet volume scales according to $V \propto \left(\frac{P_d}{P_c}\right)^{1/3}$.

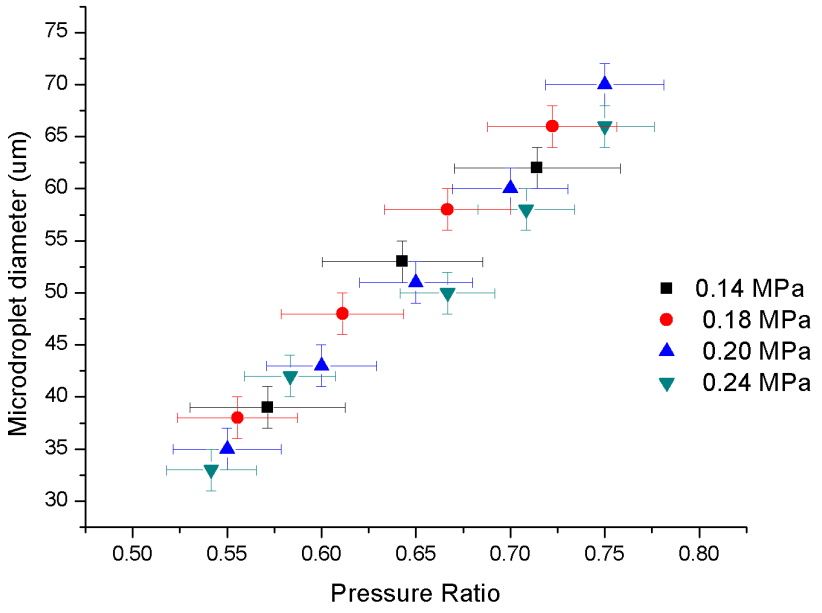

Figure 4-10 *Microdroplet diameter as a function of the pressure ratio of the dispersed and the continuous phases. Different data sets corresponding to continuous phase pressure ranging from 0.140 MPa to 0.240 MPa all collapsed on the same master curve.*

This linear dependence between the microdroplet diameter and the pressure ratio has also been observed by Ward *et al*.[76] using a flow focusing design with different dimensions[15]. These results suggest two things: 1) the linearity between the microdroplet size and the pressure ratio does not depend on a set of specific geometrical parameters, which means that P_d and P_c are relevant parameters to control the microdroplet size; and 2) the pressures applied to the continuous and dispersed phase are not linearly proportional to the flow rates of the two phases. This statement is further supported by the observation of backflow in *Figure 4-9* and *Figure 4-12*. In these cases, the dispersed phase flow rate is negative, even though a positive pressure is applied. A simulation of the flow-focusing geometry done by Dupin *et Al.* revealed the presence of two eddies in the disperse phase in the vicinity of the interface with the continuous phase[77]. This small turbulence could explain the non-linearity between the flow rates and the applied pressures.

4.4. Microdroplet production throughput

In order to be relevant for biomedical research, the proposed encapsulation process must be able to produce a sufficient amount of microcapsules. In typical in vivo animal studies, 250 000 to 500 000 cells are injected in a mouse, and 1 million cells are injected in a rat. Furthermore, many animals are required to obtain statistically sound results. On the other hand, the encapsulation process should be as quick as possible to maximize cell viability. Consequently, the throughput (or frequency of production) of the microcapsules is very important. The device operation parameters were thus investigated to optimize the production of microdroplets.

Firstly, the impact of the absolute values of P_c and P_d was assessed. The droplet throughput was measured on-chip while P_c and P_d were increased proportionally (between 0.040 MPa and 0.240 MPa) to keep the droplet diameter constant. The measured throughput was expressed as a function of P_c (see *Figure 4-11*). It was observed that the whole range of droplet diameters (from 20 to 80 µm) is not accessible for any values of P_c: 80 µm droplets could only be produced for $0.040\ MPa \leq P_c \leq 0.160\ MPa$; 60 µm droplets for $0.040\ MPa \leq P_c \leq 0.200\ MPa$; and 40 µm droplets for $0.120\ MPa \leq P_c \leq 0.240\ MPa$. As mentioned previously, the value of Γ_{max} (where the dripping transitions to jetting) decreases as P_c increases. As a result, the maximal microdroplet diameter also decreases with increasing P_c. All data sets were found to collapse on the same master

[15] Ward *et al*. they claim that the microdroplet diameter scales with $(\Gamma)^2$. However, a closer look at their data reveals that they included data points where the droplets were larger than the microchannel dimensions. In these cases, the droplets were significantly compressed and their measured length higher than their effective diameter. Setting aside these altered data points, the microdroplet diameter scales linearly with Γ.

curve and indicate that higher values of P_c and P_d produces microdroplets at an exponentially faster rate.

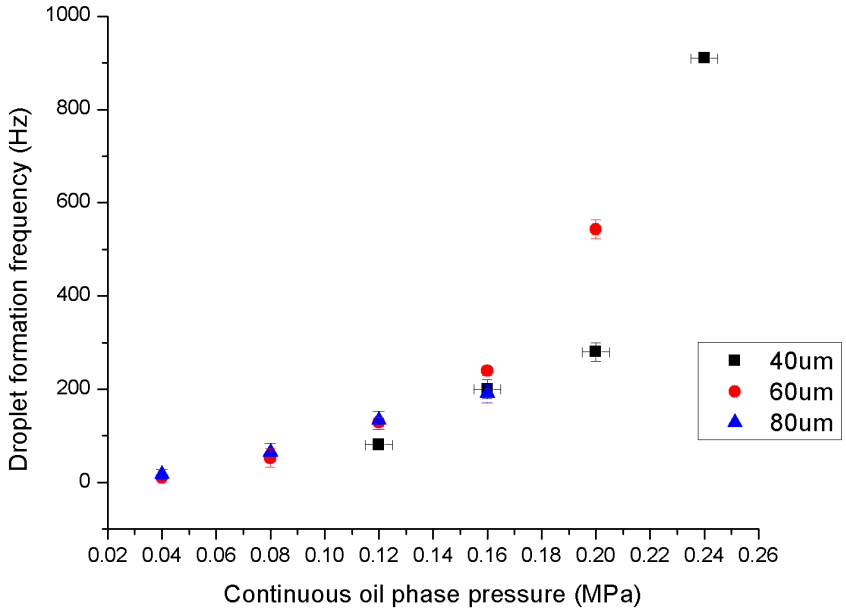

Figure 4-11 *Formation frequency of 40 µm, 60 µm and 80 µm microdroplets for increasing values of* $\boldsymbol{P_c}$ *while Γ is kept constant.*

To assess the impact of surfactant, the throughput was measured for SPAN 80 concentrations of 1%, 2% and 3%. It was observed that an increase in surfactant concentration leads to a decrease of $P_{c_{max}}$, which favors jetting and limits throughput (see *Figure 4-12*). For low value of surface tension, capillary instabilities (which cause the collapse in the second stage of the formation mechanism) are almost inexistent. Consequently, the neck does not break as quickly and is more prone to extend and form a jet. We found that $P_{c_{max}} = 0.240\ MPa$ for a solution of 2% SPAN 80 and $P_{c_{max}} = 0.200\ MPa$ a solution of 3% SPAN 80.

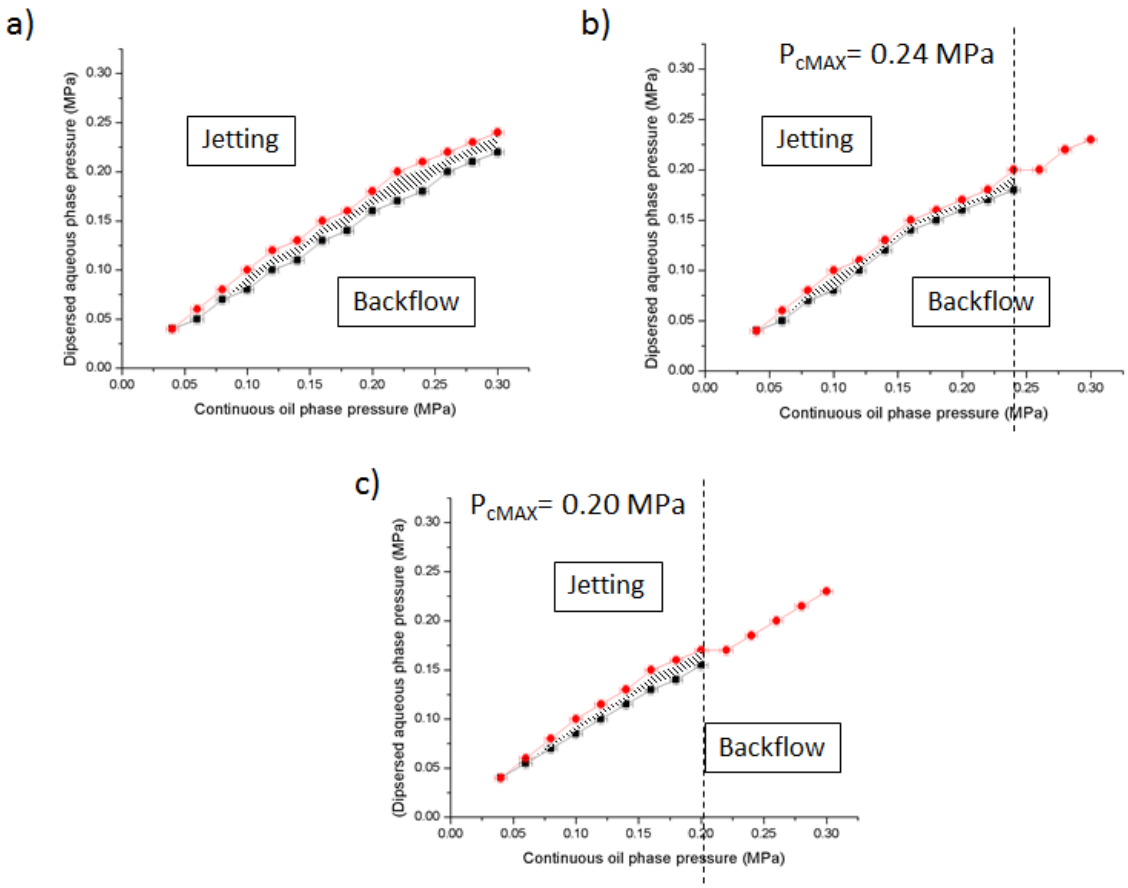

Figure 4-12 *Phase diagrams illustrating the droplet production regimes for a) 1% SPAN 80; b) 2% SPAN 80; and c) 3% SPAN 80. The lower line indicates the transition from backflow dripping, and the upper line indicates the transition from dripping to jetting. The hatched region represents the range of pressures for which the dripping regime is obtained (error bars are contained within the symbols).*

A second experiment concerning the effect of surface tension on the droplet formation mechanism revealed a surprising effect. This time, the throughput was measured directly on-chip while the surfactant concentration was varied from 1 % to 3%. It was found that for constant values of P_c and P_d (0.180 MPa and 0.100 MPa respectively), a higher surfactant concentration generates an increased throughput (see *Figure 4-13*). This suggests once more that surface tension opposes the deformation of the dispersed phase in the first stage of droplet collapse. As surface tension is decreased, the deformation rate increases, which generates smaller droplets at a higher throughput. The frequency of production was found to stabilize between 2.5 % and 3 % SPAN 80. At this point, the surfactant has reached its critical micellar concentration and surface tension is at its minimal value.

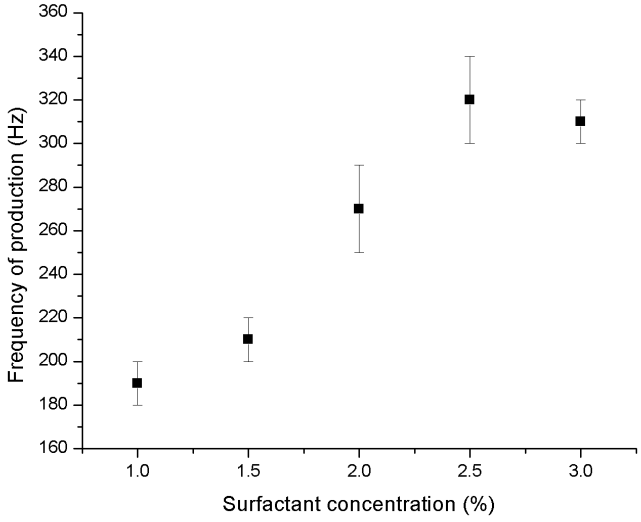

Figure 4-13 *Microdroplet production throughput for increasing concentration of SPAN 80 while pressures are maintained constant.*

In light of all these results, the surfactant concentration has two opposite effects on droplet production: 1) a reduced surface tension increases the deformation rate in the first stage of the droplet breakup mechanism, which yields smaller droplets and an increased throughput (see *Figure 4-13*); and 2) a reduced surface tension decreases capillary instabilities in the last stage of the droplet breakup mechanism, which limits the maximal throughput that can be achieved because of the jetting effect (see *Figure 4-12*). To assess which of these effects is stronger, the maximal frequency of production was measured for different size of droplets at different surfactant concentrations. It was found that a higher surfactant concentration yields a lower throughput for all droplet sizes tested (see *Figure 4-14*). This suggests that the dripping to jetting transition is the strongest factor limiting throughput. Furthermore, the maximal throughput was found to decrease with droplet diameter. For a SPAN 80 concentration of 1%, 56 µm droplets were produced at 920 ± 20 Hz whereas 84 µm droplets were produced at 320 ± 10 Hz. The maximum throughput of droplets smaller than 56 µm was not investigated because it corresponded to values of P_c higher than 0.300 MPa, which is the pressure limit of the setup. However, by strengthening the interface between the tubing and the microfluidic device, microdroplets could be produced at an even higher frequency.

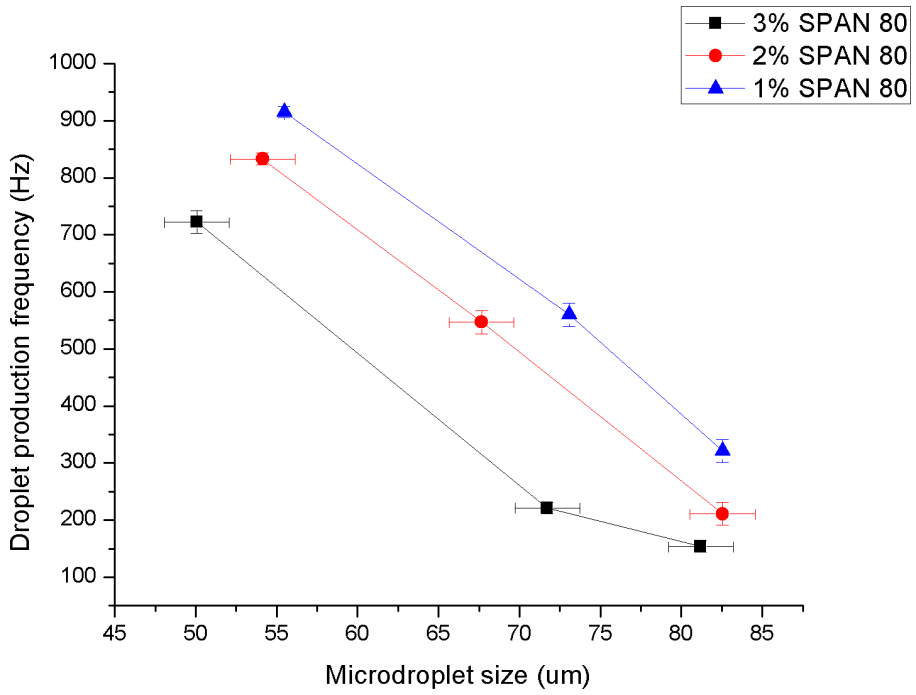

Figure 4-14 *Maximal droplet production frequency as a function of microdroplet size for different concentrations of SPAN 80.*

4.5. Summary

As can be seen in the detailed discussion above, there are many parameters to consider in order to produce monodisperse microdroplets of a specific size at high throughput. The agarose concentration should be chosen to minimize viscosity while maximizing mechanical strength. For this reason, an agarose concentration of 2 % was mostly used in our experiments because it yielded microdroplets that could sustain the resuspension to an aqueous solution (see Chapter 5 – Section 2), and allowed droplet formation via the dripping regime even at high pressures (up to $P_c = 0.24\ MPa$). To increase the throughput even more, the agarose concentration can be lowered gradually and the corresponding mechanical strength of the microcapsules investigated.

As mentioned in Section 4.3, the microdroplet size (which ranges from 30 µm to 80 µm) varies linearly with the pressure ratio $\Gamma = \frac{P_d}{P_c}$. However, depending on the absolute values of both pressures, some microdroplet sizes cannot be produced. At higher pressures, only smaller microdroplets can be produced while at lower pressures, only larger microdroplets can be produced. As a reference, Table 2 presents the values of P_c for the generation of different

microdroplet sizes. Once P_c is set, $P_d$must also be adjusted to obtain the appropriate pressure ratio Γ. Since the pressures in the vicinity of the interface between the two phases depend on the pressure drops across both inlets, these values are only valid for the specific parameters used (device geometry, fluid viscosities and surface tension). However, these values can serve as a reference for comparison after the modification of any of the parameters.

Microdroplet size (µm)	Range of P_c (MPa)	Pressure ratio Γ
40	$0.120 \leq P_c \leq 0.240$	0.57 ±0.04
60	$0.040 \leq P_c \leq 0.200$	0.71 ±0.04
80	$0.040 \leq P_c \leq 0.160$	> 0.75

Table 2 *The range of $\boldsymbol{P_c}$ for which it is possible to generate 40 µm, 60 µm and 80 µm microdroplets, as well as the pressure ratio $\boldsymbol{\Gamma}$ corresponding to each of the microdroplet diameters.*

Chapter 5 – GELATION OF AGAROSE MICROCAPSULES IN CONTINUOUS FLOW

5.1. Gelation temperature

The next task was to determine if the agarose capsules could be gelled on-chip. For this purpose, the serpentine channel temperature must be decreased below the agarose gelation temperature. To ensure that the proposed platform is able to gel the agarose microcapsules on-chip, the gelation temperature of agarose microcapsules at different concentrations had to be investigated. This experiment was not intuitive to perform however, because no obvious visual differences were found between the droplets in their sol and in their gel state. Consequently, a peculiar property of agarose was used, namely syneresis or "weeping". It was confirmed in the literature that agarose gels are prone to expel the water they contain when a stress is applied to them[22]. Consequently, microcapsules with diameters larger than the channel height (which was 45 µm for this experiment) were produced. When the droplets gelled, they were compressed by the geometrical dimensions of the device and expelled some of their water content. This phenomenon caused the gelled agarose core to become quite visible and the gelation temperature could thus be measured (see *Figure 5-1*).

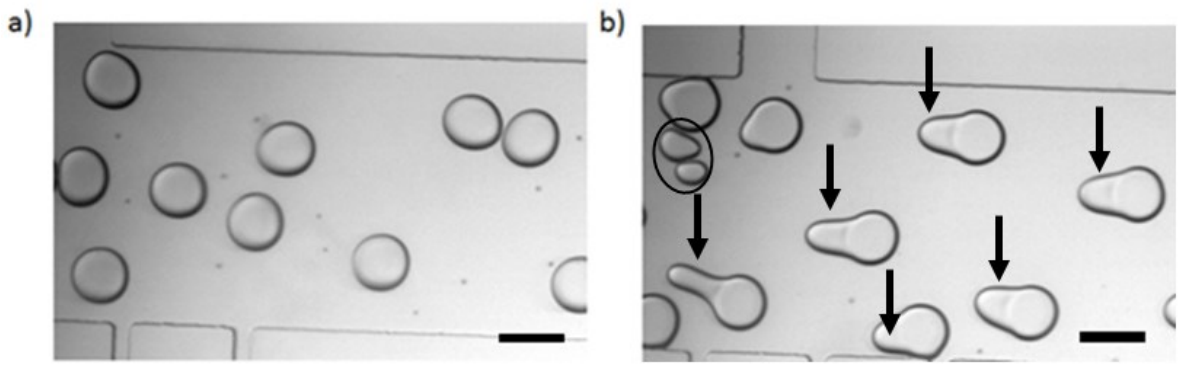

Figure 5-1 *a) a serpentine temperature higher than the agarose gelation temperature yields liquid microdroplets. b) a serpentine temperature lower than the agarose gelation temperature yields gelled microcapsules weeping because of the geometrical constraints. The expelled water content is identified with the arrows. The smaller droplets (circled) are liquid water droplets that have been completely extracted from gelled agarose microcapsules (all scale bars = 80 µm).*

To isolate the effect of agarose concentration on gelation temperature, other parameters influencing the gelation processes were controlled. Consequently, the values of P_c and P_d were adjusted so that the diameter of the microcapsules and their traveling speed remained at the constant values of 70 µm and 3 ± 0.4 mm/s respectively (a detailed discussion on droplet speed

control follows). To measure the on-chip temperature, a thermistor was introduced in the vicinity of the serpentine via a punched hole. Previous device characterization revealed that the temperature at this point did not to differ from the serpentine temperature by more than 3°C.

Using the method described above, the gelation temperature agarose microcapsules with concentration ranging from 2% to 3.5% were measured (see *Table 3*). All measured gelation temperatures were significantly higher than 6°C, which is the minimal serpentine temperature attainable by the proposed system. At a concentration of 3.5%, the measured gelation temperature was 24 ± 1°C, which explains why higher concentrations of agarose did not allow stable microdroplet production (see *4.1. Preliminary* experiments).

Agarose concentration (%)	Gelation temperature (°C)
2	17.5 ± 0.8
2.5	19.6 ± 0.9
3	22.4 ± 0.7
3.5	24 ± 1

Table 3 *Gelation temperature of 70 µm sized agarose microcapsules for different agarose concentrations.*

To confirm that the weeping observed was not an out-of-equilibrium phenomenon that occurred before the gelation temperature was reached, the microcapsules were collected and put in the fridge at 4°C for 3 hours. The microcapsules were then visualized on a glass slide. Without any external stress applied, the microcapsules did not present any visible phase separation. Furthermore, some of the microcapsules appeared to have coalesced (see *Figure 5-2*a). However, when a cover slip was applied to the sample, the microcapsules were compressed and expelled their water content in a very similar way than what was observed on-chip. This thus confirmed the accuracy of the method proposed above. Furthermore, the microcapsules that previously appeared to have coalesced were found to be distinct agarose microcapsules sharing a common water shell.

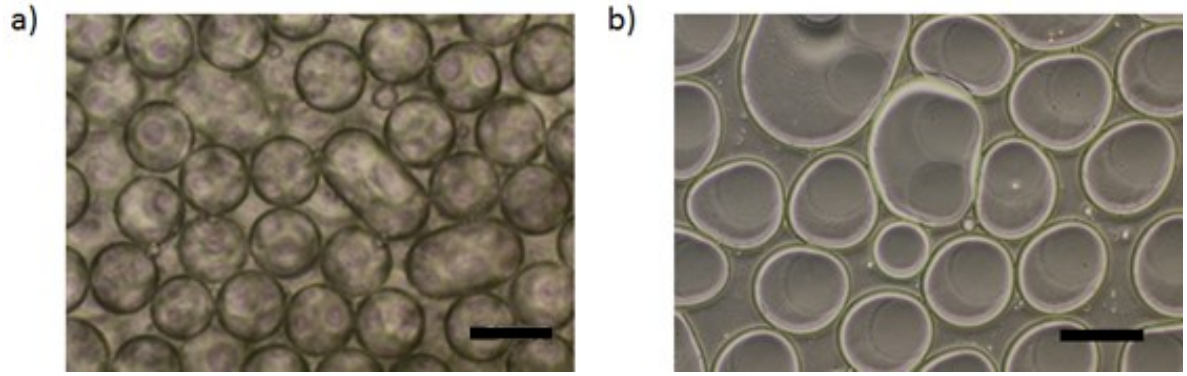

Figure 5-2 *Agarose microcapsules gelled for 3 hours at 4°C a) without coverslip and b) with coverslip. The stress imposed on the microcapsules by the coverslip forces them to expel some of their water content (scale bar = 80 µm).*

5.2. Gelation time

The three main parameters affecting gelation are temperature, gelation time and agarose concentration. Since the ability to quench the microcapsules well below their gelation temperature had already been proven, the capacity to control gelation time was investigated next. As mentioned before, the length of the serpentine was fixed to 144 mm. Consequently, the gelation time needed to be control via the droplet speed. The values of P_d and P_c were increased proportionally (between 0.040 MPa and 0.240 MPa) to keep droplets diameter constant, and the resulting traveling speed of the droplets was measured on-chip. The experiment was repeated for droplets with diameter of 40 µm, 60 µm and 80 µm (the channel height was 90 µm). The measured traveling speed was expressed as a function of P_c. It was found that for a constant droplet diameter, the droplet speed increases linearly with P_c (*Figure 5-3*). This suggests that the microdroplets are being dragged, or carried, by the oil phase and adopt its velocity (which varies linearly with P_c). It was also observed that larger microdroplets travel slower than their smaller counterparts. This is probably because their larger size exposes them to lower velocity stream lines in the oil carrier fluid. The measured traveling speeds ranged from 0.7 ± 0.1 mm/s to 15.3 ± 0.6 mm/s. For a serpentine channel length of 144 mm, these values correspond to gelation times ranging from 200 ± 10 s to 9.4 ± 0.4s. In close agreement with the results presented in Chapter 4 – Section 4, 80 µm droplets could only be produced for $0.040\ MPa \leq P_c \leq 0.120\ MPa$; 60 µm droplets for $0.040\ MPa \leq P_c \leq 0.200\ MPa$; and 40 µm droplets for $0.120\ MPa \leq P_c \leq 0.240\ MPa$.

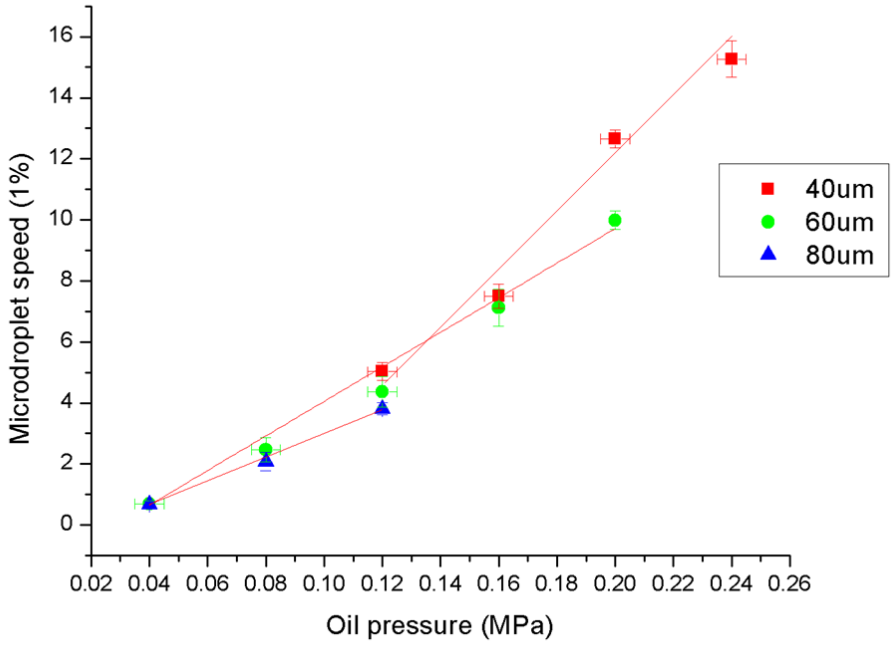

Figure 5-3 *Microdroplet traveling speed as a function of the oil phase pressure.*

As discussed in the previous section, operating the device at higher values of P_c and P_d is desirable to maximize throughput. However, the last results showed that higher values of P_c imply faster droplet traveling speed, and thus reduced gelation time. As a final characterization of the agarose microcapsule gelation, the impact of reduced gelation time on microcapsule gelation was investigated. To optimize the gelation as much as possible, the serpentine temperature was maintained at its minimal temperature of 6°C. In order to cover the maximal throughput of the device, a concentration of 1% surfactant was used. The values of P_c and P_d were once again adjusted to keep the microdroplet diameter constant. However, their absolute value was increased and the resulting increasing on-chip droplet traveling velocities were measured. For a given microdroplet diameter, three different gelation times were investigated ranging between 9 ± 1s and 62 ± 1s, thus spanning the higher throughput range of the device. The gelled microcapsules were collected for 30 minutes in 1mL of phosphate buffered saline (PBS) maintained at 37°C. The sample was centrifuged at 217g for 3 minutes, the oil supernatant was removed and the microcapsules were resuspended in 5 mL of PBS. This rinsing procedure was repeated three times to ensure complete oil removal. Three microdroplet diameters (~40 µm, ~60 µm and ~80 µm) were produced, which yielded a total of nine samples. After off-chip oil removal and resuspension in PBS, it was

observed that the cocoons aggregated together (see *Figure 5-4*a). These aggregates are undesirable because: 1) they could cause an adverse reaction if injected in an animal for an in vivo study; 2) they are incompatible with flow cytometry measurements since they would clog the channels of the flow cytometer. To separate the cocoons, the microcapsules were pipetted up-and-down ten times with the pipette tip slightly pressurized against the vial's bottom. The shear stress generated by this technique was found to be sufficient to separate the microdroplets (*Figure 5-4*b).

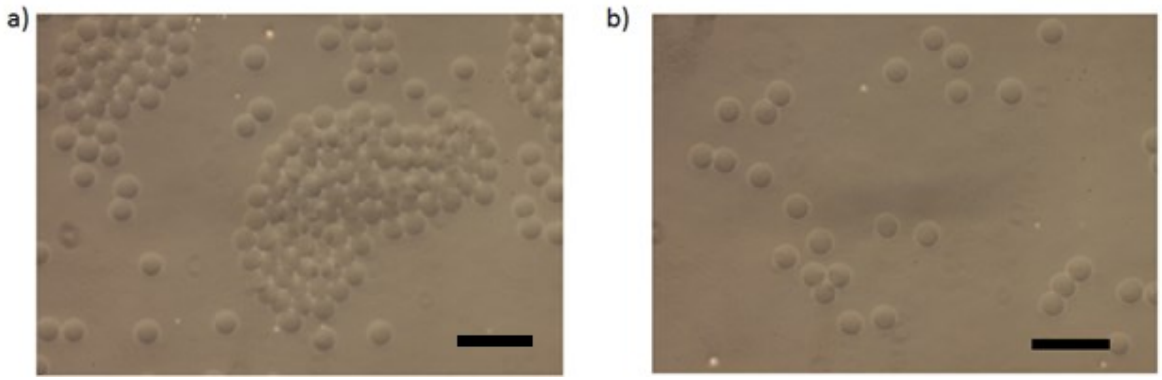

Figure 5-4 *Agarose microcapsules gelled on-chip. a) After off-chip oil removal and resuspension in PBS, the microcapsules form aggregates; and b) pipetting up-and-down imposes a sufficient shear stress to separate the microcapsules (scale bar = 200 µm).*

Once the microcapsules were nicely separated, the presence of small, oddly shaped microcapsules was noted (see *Figure 5-5*). However, the on-chip microcapsule production had been thoroughly supervised and no microdroplet presented these features on-chip. Consequently, these microdroplets were damaged by the resuspension procedure. The shear stress imposed by up-and-down pipetting must have compressed them into smaller denser capsules, which also explains why they appear brighter under phase contrast microscopy.

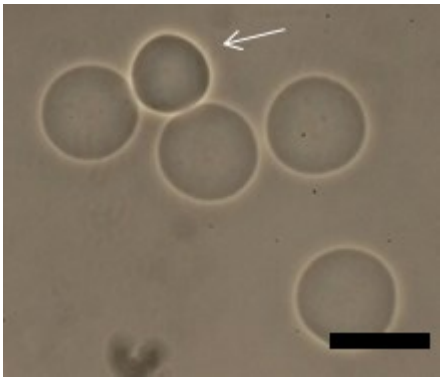

Figure 5-5 *The resuspension procedure damages some of the microcapsules (indicated by the arrow) (scale bar = 60 µm).*

For each sample, 5 images each containing between 21 and 44 microcapsules were considered. The percentage of damaged microcapsules was averaged over the 5 images. It was observed that shorter gelation times typically imply a higher percentage of damaged microcapsules (see *Table 4*). The values ranged from 2 ± 1% to 10 ± 2%. This is not surprising considering that the sol-gel transition of a polymer is a progressive, percolative process. Typically, the mechanical strenght of a polymer gel increases with the number of cross-links in its networks until the gelation process is complete. The increasing number of damaged microcapsules for a reduced gelation time thus suggests that the mechanical strenght had not yet reached its maximum value. However, a precise value of the gelation time required to minimize the percentage of damaged microcapsules could not be found due to the inconsistency of the shear stress applied via pipette resuspension. Ultimately, the mechanical strength of the microcapsules could be measured as a function of gelation time using an atomic force microscope[78]. However, this method is very time intensive and probably not worth it since the mechanical strength of the microcapsules is already sufficient to allow ≥90% of the capsules to be resuspended in an aqueous solution without losing their sphericity. Furthermore, the presented method could still be improved by: 1) increasing the length of the serpentine channel, which scales linearly with gelation time; 2) resuspending the microdroplets on-chip using the phase-transfer module.

Pre-gelation size (um)	Gelation time (s)	Post-gelation size (um)	Damaged microcapsules
43	9 ± 1	42	8 ± 3%
43	11.2 ± 0.5	41	2 ± 1%
42	19 ± 1	41	1.8 ± 0.9%
58	12.5 ± 0.6	59	10 ± 2%
59	20.7 ± 0.7	59	8 ± 2%
60	44.3 ± 0.9	59	6 ± 4%
79	22.4 ± 0.9	78	8 ± 2%
79	29. 4 ± 0.6	80	4 ± 2%
79	62 ± 1	79	2 ± 1%

Table 4 *Characteristics of the nine samples of agarose microcapsules gelled on-chip.*

The diameter of the resuspended microcapsules was measured to assess their swelling behaviour. The damaged microcapsules were easily distinguishable and were excluded from the measurement to clearly isolate the effect of swelling. The resuspended droplet diameter was not found to vary significantly from the pre-gelation microdroplet diameter, which implies that the final microdroplet size can be reliably adjusted on-chip, without having to compensate for swelling or

shrinking of the microcapsules (as long as the resuspension medium is PBS). Furthermore, the size polydispersity of the resuspended microcapsule was below the resolution limit of the setup once again. Once again, the average width of the halo was measured to be 2 µm (see *Figure 5-6*).

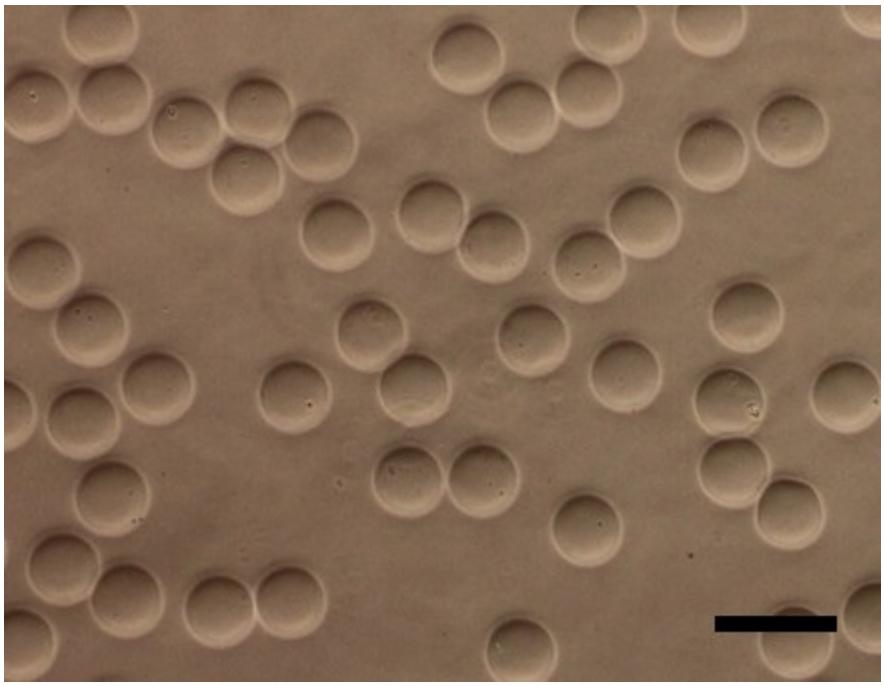

Figure 5-6 *60 µm monodisperse agarose microcapsules gelled on-chip and resuspended off-chip in PBS (scale bar = 100 µm).*

Chapter 6 VIABLE AND CONTROLLED CELL ENCAPSULATION IN AGAROSE MICROCAPSULES

6.1. Average cell occupancy

In the previous sections, it was demonstrated that the proposed platform produces monodisperse agarose microcapsules of controlled diameter (from 20 µm to 80 µm) at high throughput (from 320 Hz to 920 Hz). An important objective in this project is to ensure cell viability after the encapsulation process.

In order to encapsulate cells reliably, a single-cell suspension (without any aggregates or cell clumps) is required. In the presence of aggregates, cells are more likely to be found together and they cannot be considered as independent statistical events. Consequently, the Poisson distribution does not hold. Instead, a majority of the microcapsules are either unoccupied, or completely filled with cells (see *Figure 6-1*a). In a single cell suspension however, the probability that a given microdroplet contains a cell is completely uncorrelated to the occupancy of the previous microdroplet. Consequently, the process can be described by Poisson's distribution (see *Figure 6-1*b).

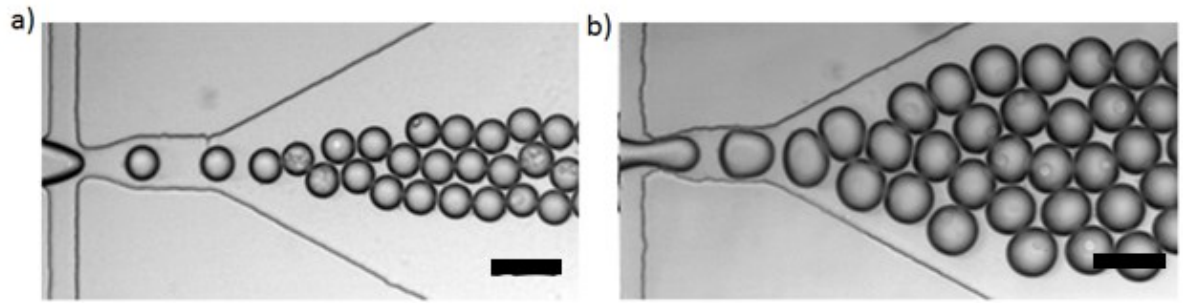

Figure 6-1 *a) cell aggregates alter the average occupancy by generating either unoccupied or overfilled microcapsules; b) a single cell suspension is ideal for control over cell occupancy (scale bar = 100 µm).*

Obtaining a single cell suspension can be tricky, since cell adhesion is a natural and essential process involved in many biological functions. However, the confluency at which the cells are detached from the plate was found to have a reproducible influence on the presence of cell aggregates. At low confluency (<30%), cells are typically isolated from each other (see *Figure 6-2*a). At higher confluencies (>30%) however, cells start connecting to each other and form multi-cellular structures (see *Figure 6-2*b). Once these bridges appear, it was observed to be increasingly difficult to obtain a single cell suspension.

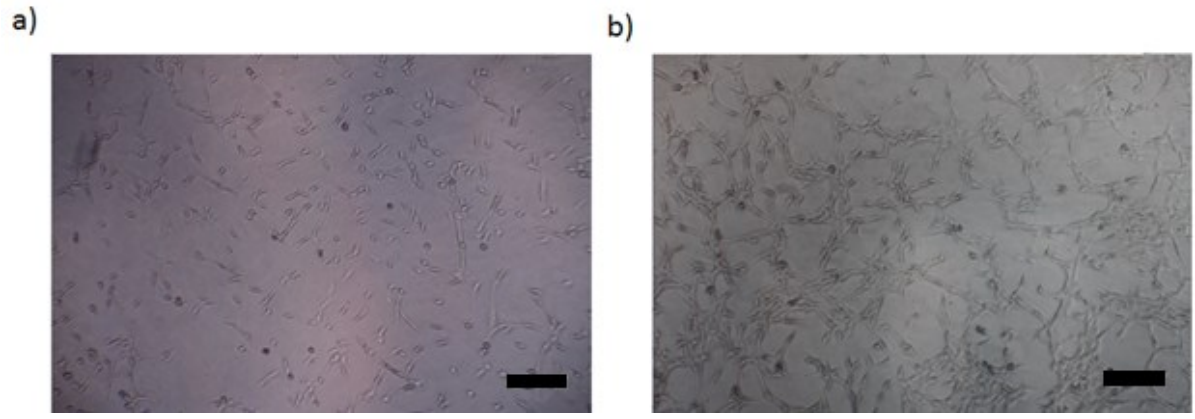

Figure 6-2 *3T3 cells adhered to a petri dish. a) At ~30% confluency, the cells are nicely isolated from each other; b) at ~50% confluency, the cells form connections and highly concentrated regions are generated (scale bar = 50 µm).*

That being said, detaching the cells at low confluency was usually not sufficient to obtain a single cell encapsulation. Cell adhesion also had to be prevented in the cell suspension prior to the encapsulation process. To do so, cells should not be suspended at a too high concentration. Furthermore, cells should be prevented from settling, since settling generates a higher cell concentration at the bottom of the vial. To do so, a rotating magnetic stir bar can be used to constantly resuspend the cells as they are settling. This option requires a sample vial that is large enough to allow the rotation of the stir bar and the addition of a magnetic stirrer to the setup. However, the availability of relevant cells for biomedical applications is often limited. Consequently, the setup must be able to accommodate small amounts of sample (<50µL). To minimize sample loss, specialized inserts are used with a residual < 2 µL. However, their size and shape are incompatible with the use of a stir bar. Another strategy is to use a density gradient medium to closely match the density of the suspension solution to the density of the cells. This option prevents cells from settling altogether, and has the added benefit of being more passive than the stir bar. To find the density of 3T3 cells, a macroscopic number of cells were suspended in 5mL of DMEM culture medium. The solution was centrifuged at 217g for 3 minutes and a visible pellet was formed, signifying that the cell density was higher than that of the solution. Optiprep[16] was then added to the solution at 5% (V/V) and the resuspension/centrifugation process was repeated. The concentration of Optiprep was slowly incremented until no pellet was produced and the cells were found to be neutrally buoyant. This occurred at a concentration of 20 ± 3 % (V/V) Optiprep, which corresponds to a density of 1.07 ± 0.2 g/mL.

[16] An isosmotic non-cytotoxic solution of 60% iodixanol in water with a density of 1.32 g/mL and a low viscosity

To prevent cell aggregation even more surely, cells can be suspended in a calcium and magnesium free phosphate buffered saline since many cell adhesion molecules rely on the presence of divalent cations to function[79]. Finally, dead cells also cause aggregation because of the nucleic acid leaking out of their damaged membrane. Consequently, special care must be taken during the cell splitting procedure in order to prevent any damage to the cells. This include: 1) minimization of trypsinization time, since trypsin will eventually cleave surface proteins of the detached cells and affect their functioning[80]; and 2) minimization of the shear stress imposed to the cells via pipetting and vortexing. In light of the above discussion, cells were suspended in a solution of 2% (m/V) ultra-low gelling agarose and 20% (V/V) Optiprep in DPBS (no Ca^{2+}/Mg^{2+}) for the next experiments.

Once a single cell concentration is obtained, the cell occupancy distribution can be predicted based on Poisson's distribution. To do so, the cell concentration is measured using a hemocytometer and expressed in cells/mL. For a given microdroplet volume *V* expressed in pL, the average cell occupancy <*N*> is given by:

$$\langle N \rangle = \frac{\#cells}{mL} \times V \times 10^{-9}. \quad (7)$$

The calculated average cell occupancy can then be compared to Poisson's distribution to predict the cell occupancy distribution (see *Figure 6-3*).

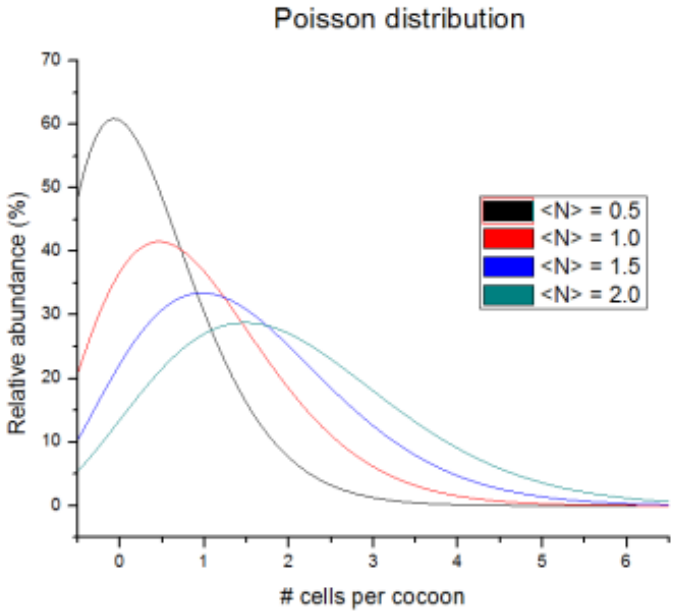

Figure 6-3 *Cell occupancy distribution for different average value of cell occupancy.*

Two experiments were performed to confirm the ability to correctly control the cell occupancy distribution. In the first experiment, cells suspended at a concentration of $(5.0 \pm 0.8) \times 10^6$ cells/mL were encapsulated in 47 µm microdroplets, which yielded a predicted value of $\langle N \rangle = 0.272$. The on-chip microdroplet diameter and the cell occupancy were compiled for one hour of operation. In total, 1506 microcapsules were counted. The cell occupancy distribution was compared to the prediction, and a very close agreement was found (see *Figure 6-4*a). Because of the low occupancy, a large majority of the microcapsules were unoccupied (82 ± 4%).

In the second experiment, cells suspended at a concentration of $(1.00 \pm 0.06) \times 10^7$ cells/mL were encapsulated in 44 µm microdroplets, which yielded a predicted value of $\langle N \rangle = 0.446$. The on-chip microdroplet diameter and the cell occupancy were once again compiled for one hour of operation. In total, 4809 microcapsules were counted. The cell occupancy distribution was compared to the prediction, and a very close agreement was found (see *Figure 6-5*b). Because of the higher occupancy, the unoccupied microcapsules were reduced to 56 ± 5%.

The results obtained in these two experiments indicate that: 1) cell occupancy distribution can be reliably controlled by adjusting cell concentration and microcapsule size; 2) cell concentrations as high as 1×10^7 cells/mL do not disrupt the droplet formation process or clog the microfluidic device; and 3) the cells do not aggregate over a period of one hour. Furthermore, the second experiment demonstrates that a cell occupancy of ~0.5 can be maintained for at least an hour. At the maximum droplet formation frequency of 920 Hz million microcapsules per hour (see Section 4.4), more than 1.5 million cells would be encapsulated per hour, which is sufficient for in vivo animal studies.

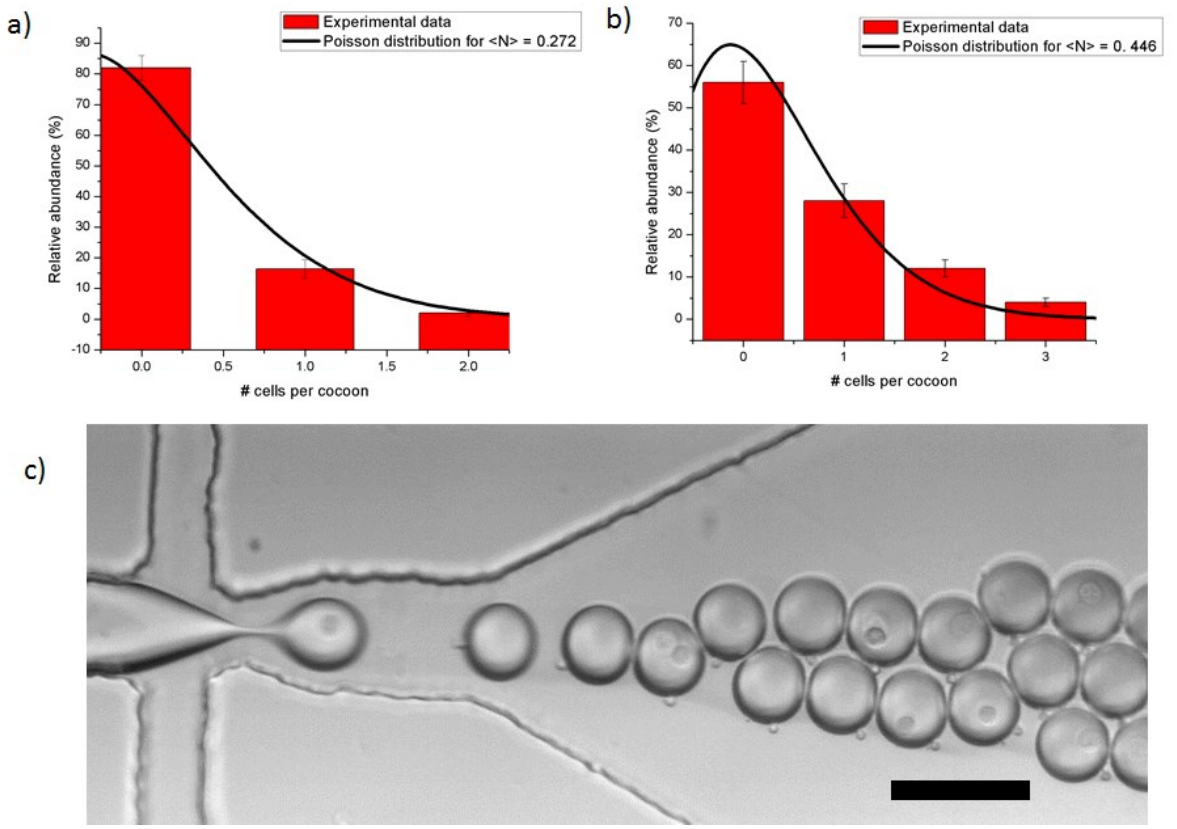

Figure 6-4 *a) cell occupancy distribution for a cell suspension of (5.0 ± 0.8) ± 10^6 cells/mL encapsulated in 47 µm microdroplets compared with the Poisson distribution for <N> = 0.272; b) cell occupancy distribution for a cell suspension of (1.0 ± 0.06) x 10^7 cells/mL encapsulated in 44 µm microdroplets compared with the Poisson distribution for <N> = 0.446; and c) the encapsulation process on-chip (scale bar = 70 µm).*

6.2. Cell protrusion

In light of the results presented above, the proposed microfluidic setup is capable of encapsulating a relevant number of cells for biomedical applications. However, a peculiar phenomenon was found to limit the cell encapsulation rate. Typically, all cells visualized immediately downstream of the nozzle are encapsulated and nicely embedded in a microdroplet. However, as the droplets travel along the device, some cells start to protrude out of the microdroplets (see *Figure 6-5*a). Furthermore, resuspended cell-laden microcapsules sometimes show distinctive craters, marking the emplacement where a cell used to be (see *Figure 6-5*b). Most probably, the protruded cells are expelled from their microcapsule by the stressful resuspension method.

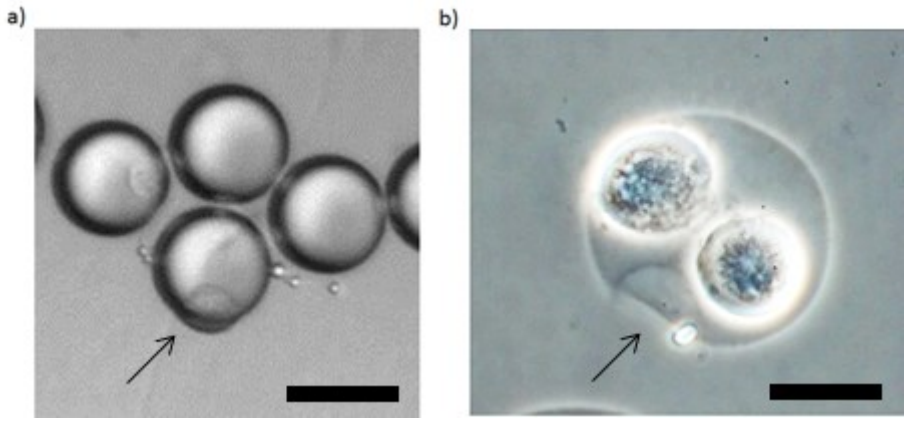

Figure 6-5 *a) Some cells protrude out of the agarose microcapsules as they travel along the microfluidic device (shown by the arrow) (scale bar = 40 µm); b) the protruded cells are expelled from the microcapsules by the resuspension method, leaving a crater behind (shown by the arrow) (scale bar = 20 µm).*

To assess the importance of cell loss via protrusion, cells suspended at a concentration of $(5 \pm 0.7) \times 10^6$ cells/mL were encapsulated into droplets of two different sizes. The first sample featured droplets with a diameter of 87 µm ($\langle N \rangle = 1.74$) and the second sample contained 58 µm droplets ($\langle N \rangle = 0.51$). The capsules were resuspended in PBS off-chip and visualized. The number of craters n_{crater} and the number of encapsulated cells $n_{enc.}$ were counted for each sample. The cell protrusion percentage *P* was then calculated following:

$$(8) \quad P = \frac{n_{crater}}{n_{crater}+n_{enc.}}.$$

For the 58 µm microdroplets, the results from 10 images each containing 11 cells in average were compiled and yielded an average protrusion of 18 ± 4 % (see *Figure 6-6*a). For the 87 µm microdroplets, the results from 8 images each containing 28 cells in average were compiled and yielded an average protrusion of 7 ± 2 % (see *Figure 6-6*b). This suggests that larger microdroplets cause a decrease in cell protrusion, even when the average cell occupancy is significantly higher. The reason is that cells encapsulated in larger droplets have a lower probability to be encapsulated near the surface because of the reduce surface-to-volume ratio. Furthermore, the ratio of the cell volume to the capsule volume decreases for larger capsules.

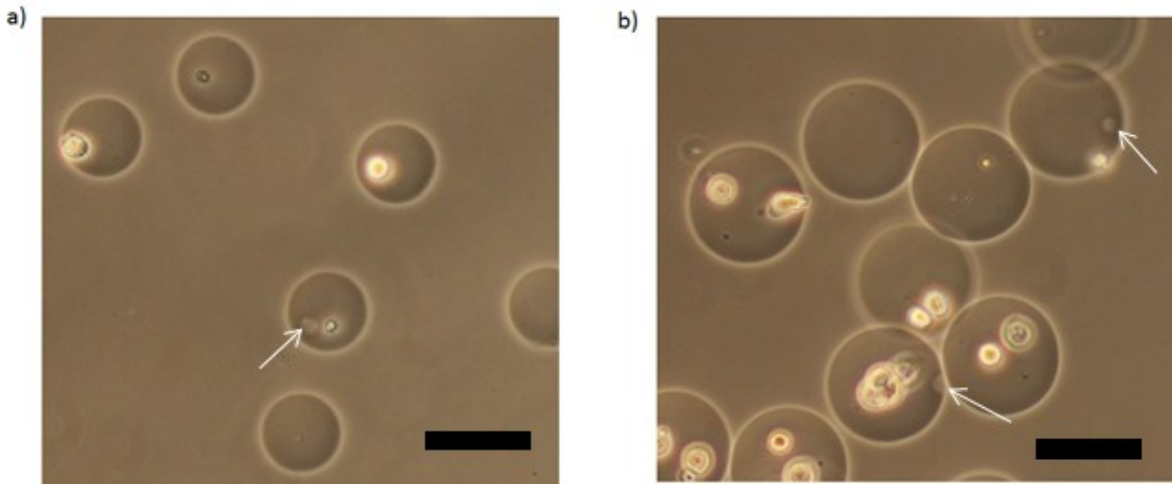

Figure 6-6 *Cells suspended at a concentration of (5.0 ± 0.7 x 10^6) cells/mL encapsulated in 58 µm (a) and 87 µm (b) agarose microcapsules. Although the cell occupancy increases for larger microcapsules, the percentage of craters left by protruded cells decreases (shown by the arrows) (all scale bars = 80 µm).*

To prevent this cell protrusion, some groups have deposited a second layer of agarose around the cell-laden agarose capsules to entrap the protruded cells[14]. However, this was not found to be necessary since cell protrusion did not compromise significantly the production of larger capsules (>50 µm). For example, the maximal throughput for 60 µm microdroplets is 800 Hz (based on *Figure 4-14*), which yields approximately 1.44 million capsules per hour at <N> = 0.5. Consequently, the effective encapsulation rate (reduced by a cell protrusion percentage of 18 %) would still be over 1 million cells per hour, which is still relevant for biomedical applications.

To confirm that the cells remaining after the resuspension were still embedded within the capsules and not simply resting on the surface, confocal microscopy was used. To make the agarose capsules fluorescent, 200 nm fluorescent microspheres (Life technologies) (excitation 580nm; emission 605 nm) were used. The microspheres were centrifuged and the supernatant was removed. The microspheres were then resuspended in DPBS to rinse off the original solution in which they were suspended, and sonicated for 60 minutes to reduce aggregates. The microsphere suspension was mixed with Optiprep and agarose 3% in DPBS to form a final solution of 2 % agarose, 20% Optiprep and 6.37 x 10^{11} microspheres/mL in DPBS. Wheat germ agglutinin (WGA) was used to stain the cell membrane. Following detachment, the cells were resuspended in 1 mL of DMEM culture medium and 10 µL of WGA was added. The cell suspension was incubated for 25 minutes at room temperature in the dark. Afterwards, the excess dye was rinsed off and the cells were resuspended in the agarose solution described above. The cells were encapsulated in 45 µm

microcapsules which were resuspended in PBS off-chip. The cell-laden capsules were then visualized under a confocal microscope. Two-dimensional planes were acquired and stacked to reconstruct a three-dimensional image of a cell enclosed in an agarose capsule (see *Figure 6-7*). The red fluorescent signal produced by the microspheres clearly delimits the agarose capsule whereas the green signal from WGA undoubtedly locates the cell within the boundaries of the capsule. Although time consuming, this technique could be used to directly probe the position of the cells within the capsules, and assess the number of protruded cells more precisely.

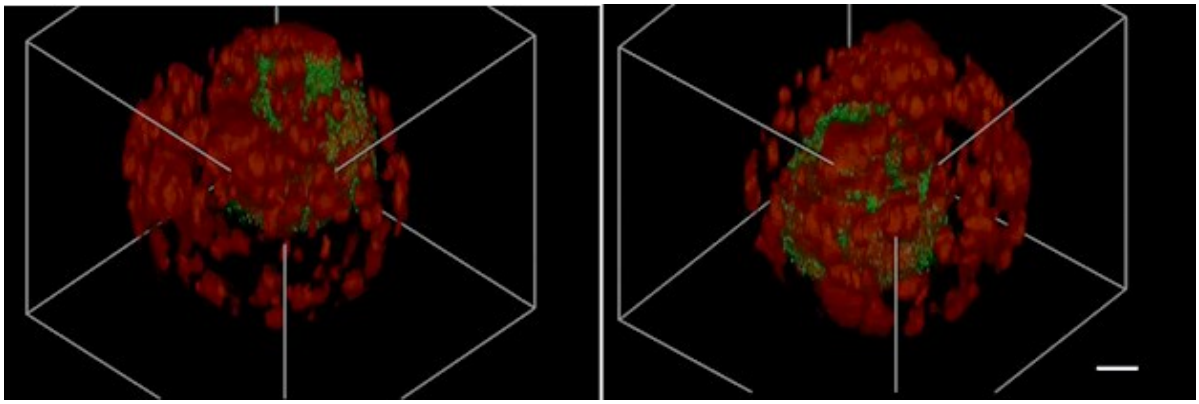

Figure 6-7 *Confocal image of a cell embedded in an agarose microcapsule. Fluorescent microspheres were encapsulated in the microcapsule to visualize the agarose network and WGA was used to stain the cell membrane (scale bar = 6 µm).*

6.3. Cell viability

Finally, to confirm that the proposed method is biocompatible, the viability of the encapsulated cells was investigated using a live/dead kit for mammalian cells (Life technologies). The kit included two dyes: Calcein AM and ethidium homodimer-1 (EthD-1). Calcein AM is cell permeating and virtually non-fluorescent in its native state. However, intracellular esterase[17] activity converts calcein AM to the intensely green-fluorescent calcein (excitation 494 nm; emission 517 nm). Consequently, live cells are easily distinguished by the ubiquitous green signal. On the other hand, EthD-1 only permeates damaged cell membranes and undergoes a 40-fold fluorescence enhancement upon binding to nucleic acids (excitation 528 nm; emission at 617 nm). As a result, EthD-1 labels the nucleus of dead cells. Since EthD-1 weakly fluoresces in its native state, it is important to optimize the dyes concentration to achieve distinct labeling of live and dead cells. To do so, 3T3 fibroblast cells were encapsulated in 2% agarose microcapsules, and resuspended in a 70% methanol solution in DI water to kill them. After 30 minutes, the cell-laden microcapsules were

[17] The splitting of esters into an acid and an alcohol via hydrolysis

resuspended in PBS and both dyes were added at a concentration of 1 µM. The microcapsules were then incubated 35 minutes at room temperature in the dark. To rinse off the excess unbound dye molecules and decrease background fluorescence, the sample was centrifuged 3 minutes at 217g, the PBS supernatant was extracted, and the microcapsules were resuspended in in PBS. The rinsing procedure was repeated three times, and the microcapsules were finally resuspended in PBS for visualization. The microcapsules were put on a glass slide and visualized using an epifluorescence microscope. The FITC filter cube (excitation 467 – 498 nm; emission 513 – 556 nm) was used to visualize the Calcein signal, and the TIRTC filter cube (excitation 532 – 554 nm; emission 570 – 613 nm) was used to visualize the EthD-1 signal. The results from 4 images each containing 4 cells in average were compiled and every cell appeared unambiguously red (see *Figure 6-8*).

Figure 6-8 *Optimization of the dyes concentration for the viability assay: a) phase contrast microscopy; b) green fluorescent signal; and c) red fluorescent signal. All cells appeared red (shown by the arrows) (all scale bar = 50 µm).*

Once it was demonstrated that the green fluorescence signal did not pervade into dead cells, it remained to prove that the calcein AM concentration was sufficient to stain live cells, and that the EthD-1 dye did not pervade into live cells. Immediately after the cell splitting procedure, fresh cells were resuspended in PBS and the same concentrations of calcein AM and EthD-1 were added. The same incubation and rinsing steps were also followed. This time, both fluorescence signals were stacked to the phase contrast image using ImageJ. The results from 5 images each containing 56 cells in average were compiled and 97 ± 2% of the cells were found to be uniquely emitting a green fluorescent signal (see *Figure 6-9*). These results confirmed: 1) that the calcein and EthD-1 concentrations were appropriate to avoid cross-contamination of the signals; and 2) that 97 ± 2% of the cells were alive immediately after the cell detachment process. This value would later serve as a comparison for viability assays after different processes such as encapsulation and on-chip phase transfer.

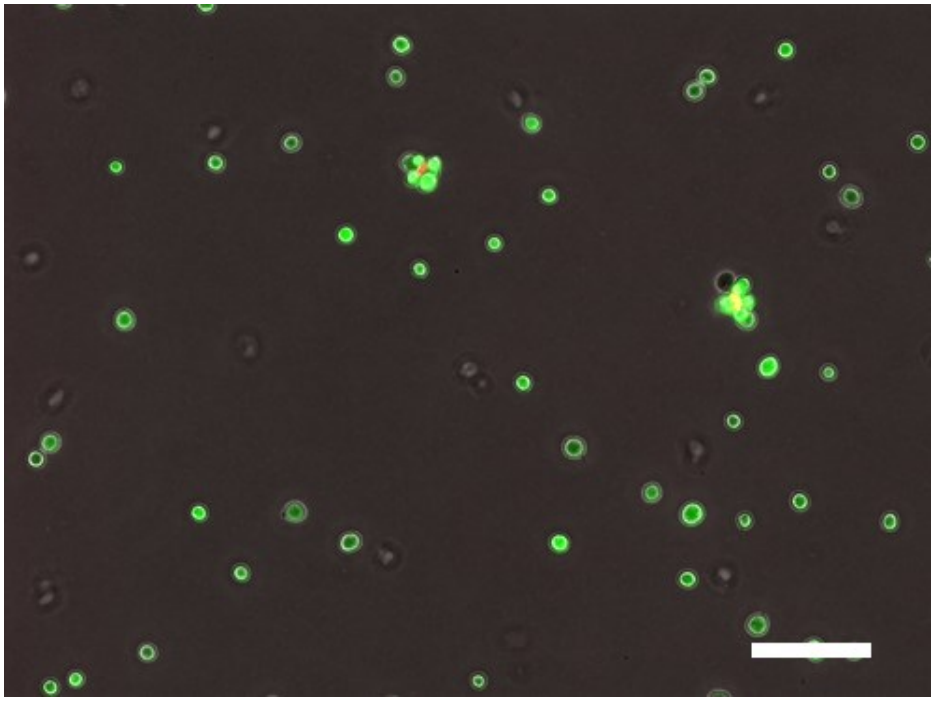

Figure 6-9 *Phase contrast, green and red fluorescent images stacked together. 3T3 cells immediately after splitting yielded a viability of 97 ± 2% (scale bar = 100 µm).*

Finally, once the dye concentration had been optimized, the viability of cells encapsulated via the proposed process was assessed. Cells were encapsulated in 80 µm capsules for 1 hour, using 1% SPAN 80 and the regular cell suspension medium. The microcapsules were collected in 1mL of DMEM culture medium maintained at 37°C to maximize cell viability. The capsules were then rinsed and resuspended in PBS off-chip. Both dyes were added to the solution at the optimized concentration of 1 µM, and the protocol described above was followed. The results from 5 images each containing 157 cells in average were compiled and yielded a viability of 92 ± 2 % (see *Figure 6-10*). The decrease in viability from the value of 97 % pre-encapsulation can be explained by a few factors: 1) the cells were suspended in a PBS-based agarose solution which lacks the fundamentals protein to preserve cell viability; and 2) the cells had no extra-cellular matrix (ECM) molecules to adhere too, which might trigger cell death because of their lack of anchorage[20].

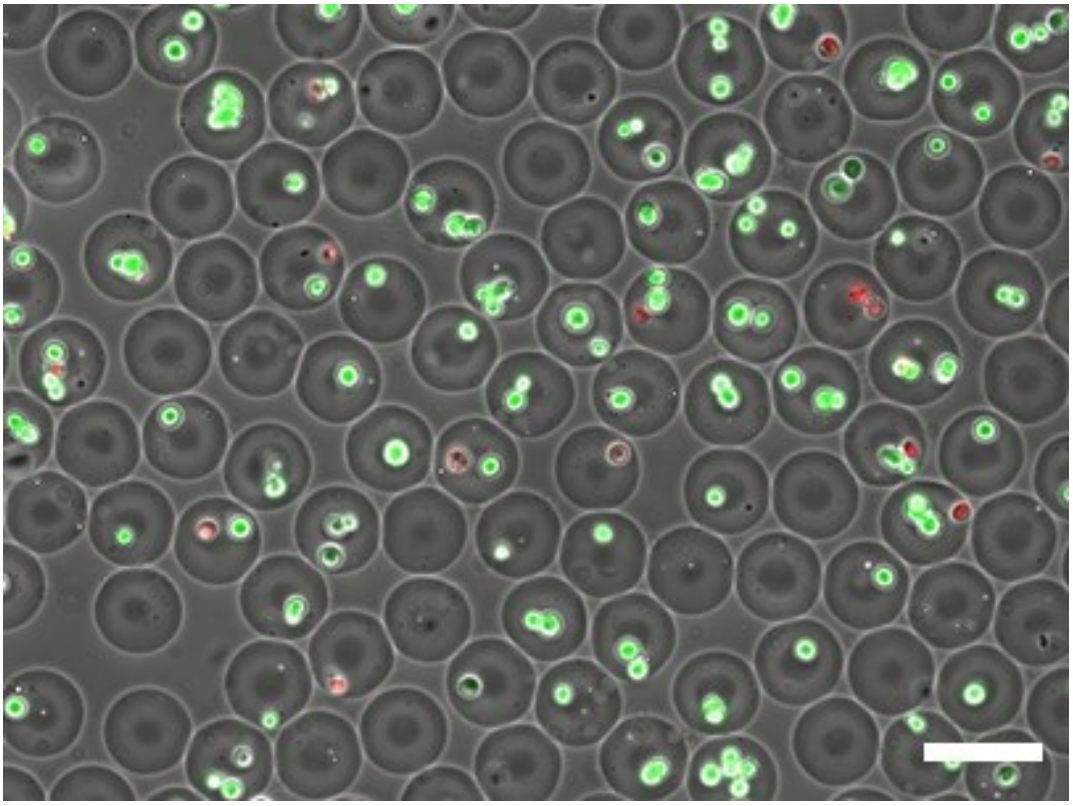

Figure 6-10 *Phase contrast, green and red fluorescent images stacked together.3T3 cells encapsulated in agarose microcapsules gelled on-chip yielded a viability of 92 ± 2 % (scale bar = 100 µm).*

Chapter 7 ON-CHIP MICROCAPSULE PURIFICATION AND OIL REMOVAL

7.1. Proof-of-concept

The platform described in Chapters 5 to 7 has been shown to allow the high-throughput encapsulation of viable cells and the continuous gelation of agarose microcapsules. To confirm the compatibility of this platform with additional on-chip downstream processing, a phase transfer module was added to the design, thus creating a three-module lab-on-a-chip (see *Figure 7-1*).

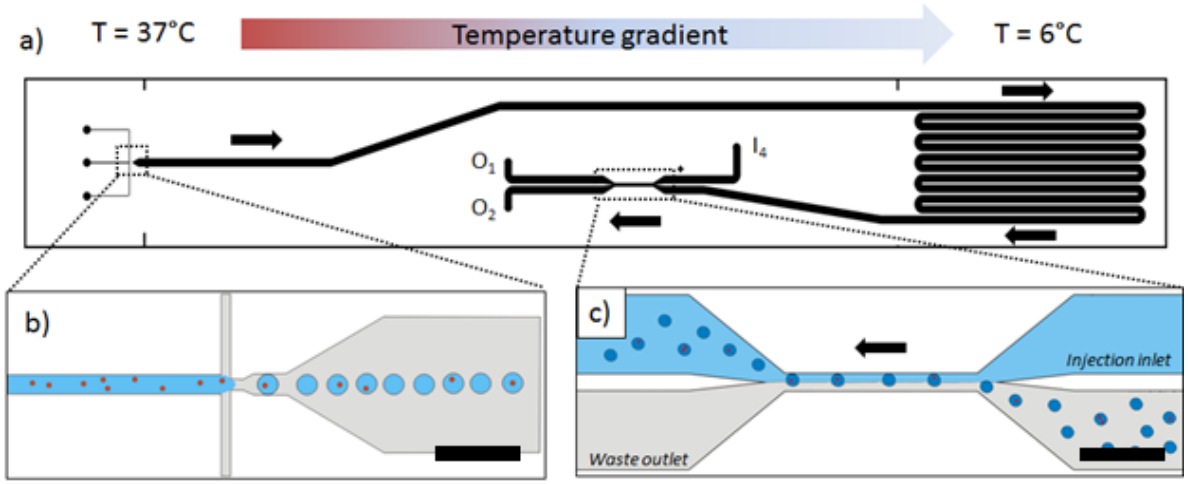

Figure 7-1 *a) Design of the three-module lab-on-a-chip; b) close-up view of the FF geometry for cell encapsulation (scale bar = 200 µm); and c) close-up view of the phase transfer module for resuspension of the microcapsules and oil removal (scale bar = 400 µm).*

In the phase transfer module, a continuous aqueous solution enters the device via an injection inlet and is forced to flow alongside the continuous oil phase inside a narrow channel with a width of 100 µm. Because the continuous aqueous phase is injected at a higher flow rate than the oil phase, the latter is compressed against the narrow channel wall and forms a thread thinner than the microcapsule diameter. This confinement is imposed to force the microcapsules to migrate from the oil phase to the aqueous phase.

The narrow channel then leads into a bifurcation which is intended for oil removal. For this purpose, a laminar interface is required between the oil and the aqueous phase. However, the native hydrophobicity of PDMS causes the oil phase to wet the PDMS, which leads to lamination of the two continuous phases (ie. the oil phase is not contained alongside the continuous aqueous phase, but rather forms a film that spans the entire top PDMS surface (see *Figure 7-2*a)). Oxygen plasma treatment could be used to increase the hydrophilicity of the device and prevent lamination,

but it is undesirable since it would oxidize the whole device, thus preventing formation of microdroplets in the FF geometry. On the other hand, a solution of $H_2O/HCl/H_2O_2$ has the same oxidizing effect on the PDMS[81], with the additional benefit of allowing selective hydrophilization of different regions of the device. The acidic solution was used to render the surface of the phase transfer module hydrophilic (see *Appendix I – Protocols for details*). After rinsing with DI water, a laminar interface was obtained between the two phases and no lamination was observed. Furthermore, by adjusting the relative pressures applied to the oil phase and the injected aqueous phase, the interface position within the narrow channel could be positioned so that the oil phase would be completely removed via the waste outlet (see *Figure 7-2*b).

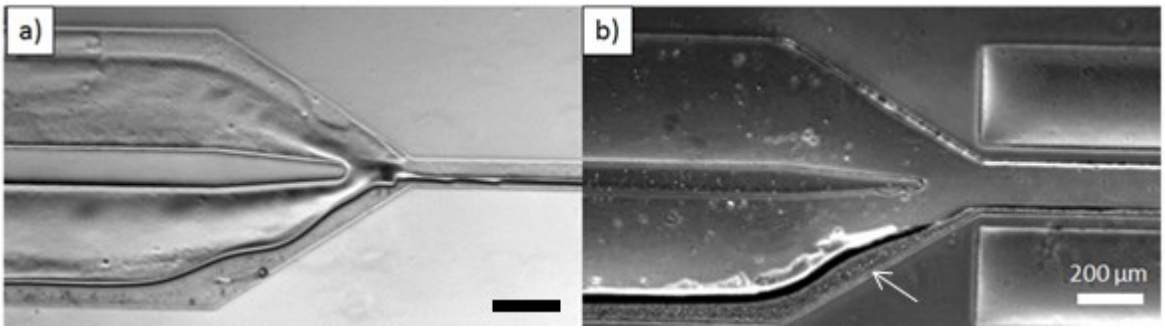

Figure 7-2 *Phase contrast microscopy image of the phase transfer module: a) the hydrophobicity of native PDMS causes lamination of the two phases; b) the acidic solution hydrophilizes the device and allows a laminar interface to be formed. The interface position was adjusted to extract the oil phase completely via the waste outlet. The oil phase is indicated by the arrow (flow direction is from right to left) (all scale bars = 200 µm).*

Once the interface was positioned correctly, 78 µm agarose microcapsules containing fluorescent microspheres were gelled on-chip and sent through the phase transfer module. The dispersed aqueous phase pressure and the continuous oil phase pressure were both set to 0.100 MPa. The behaviour of the microcapsules for different aqueous injection phase pressures P_i was observed under bright field microscopy and fluorescence microscopy using a TRITC filter cube (*Figure* ***7-3***). At $P_i = 0.100\ MPa$, almost all microcapsules remained in the oil phase and flowed through the waste outlet. At $P_i = 0.120\ MPa$, some of the microcapsules migrated towards the injected aqueous phase, although most of them still remained in the oil phase. At $P_i = 0.140\ MPa$, almost all microcapsules migrated towards the injected aqueous phase. At this point, the fluids coming out of both outlets were collected in independent tubes, and centrifuged once at 217g for 3 minutes. The microcapsules formed a clearly visible pellet because of the encapsulated microspheres. Only traces of oil were found in the collection tube whereas a significant oil layer was present in the waste tube. The supernatant was removed from both tubes and the microcapsules were resuspended in PBS. The number of microspheres in each sample was measured using a

hemocytometer. The number of microcapsules collected in the waste outlet was divided by the number of microcapsules collected in the collection outlet. This ratio was compiled for each of the 8 hemocytometer quadrants and averaged. It was found that 94.8 ± 0.5 % of the microcapsules were retrieved in the collection vial.

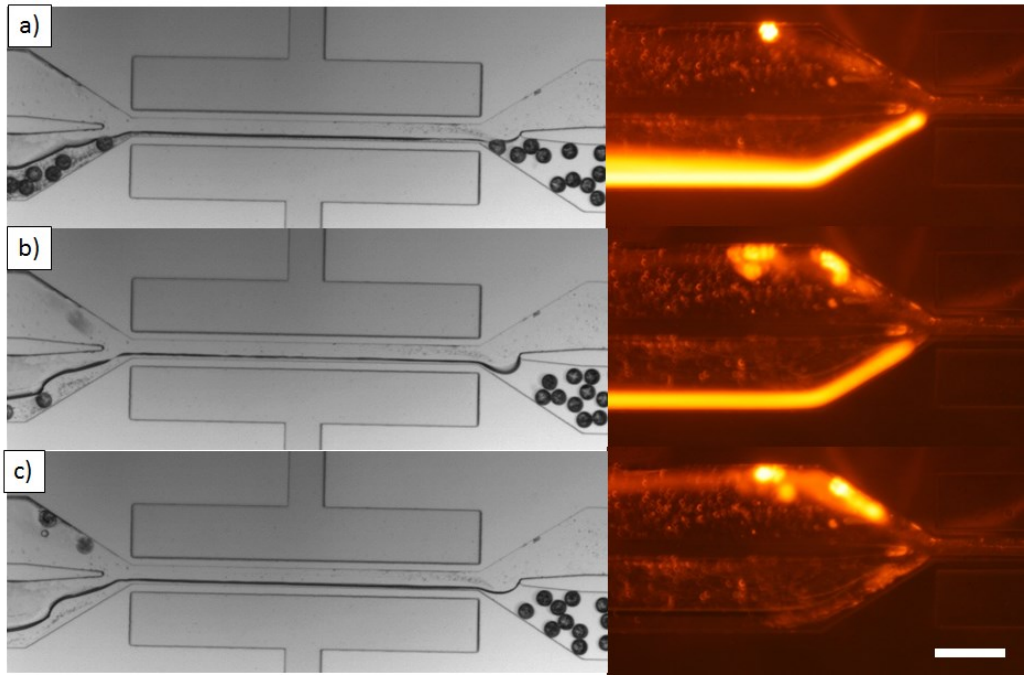

Figure 7-3 Bright field and fluorescence images of agarose microcapsules in the phase transfer module for a continuous oil phase pressure and a dispersed aqueous phase pressure of 0.100 MPa. a) At $\boldsymbol{P_i = 0.100\ MPa}$, the microcapsules remain in the oil phase; b)at $\boldsymbol{P_i = 0.120\ MPa}$, some microcapsules migrate to the aqueous phase; and c) $\boldsymbol{P_i = 0.140\ MPa}$, almost all the microcapsules migrate to the aqueous phase (flow direction is from right to left) (scale bar = 400 µm).

Similarly to the oxygen plasma treatment, an acid treated PDMS surface recovers its native hydrophobicity over the course of 1 or 2 days. Consequently, we always used our devices immediately after the surface treatment. However, long term usage should also be possible by storing the device in an aqueous solution[68].

7.2. Oil shells

To understand the source of the traces of oil found in the collection vial, the experiment was repeated with agarose microcapsules (not containing microspheres). The continuous oil phase pressure was maintained at 0.100 MPa and the dispersed aqueous phase pressure was adjusted to produce microcapsules ranging from 40µm to 90µm. The injected aqueous phase pressure was adjusted to obtain phase transfer of the microcapsules, which were collected directly on a glass

slide for immediate visualization. For all settings investigated, a significant number of microcapsules appeared unusually bright under phase contrast microscopy, which revealed the presence of a thin oil shell around the microcapsules (see *Figure 7-4*a). This suggests that the surfactant molecules at the surface of the microspheres dragged a thin oil layer through the oil-aqueous interface. However, once the collected microcapsules were centrifuged and resuspended, only traces of oil were found (*Figure 7-4*b).

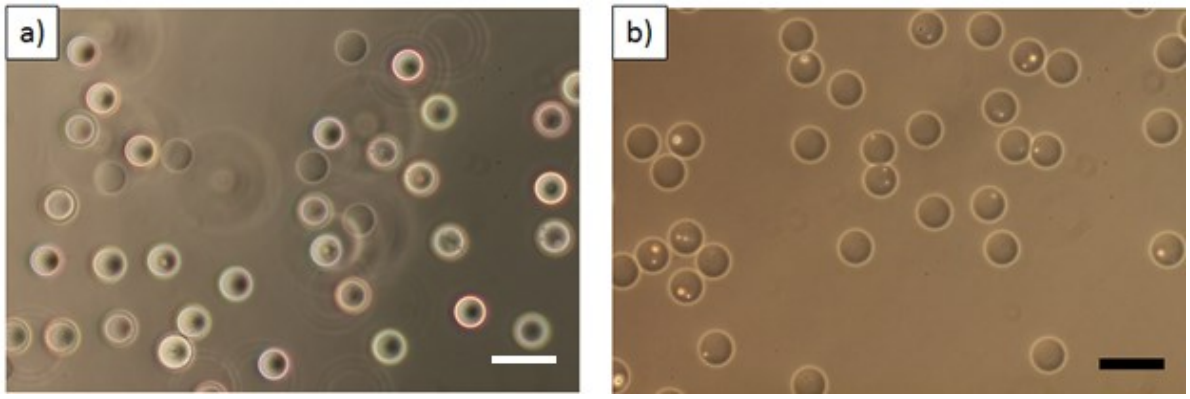

Figure 7-4 *Agarose microcapsules resuspended in PBS on-chip. a) Immediately upon exiting the device, most of the microcapsules were trapped inside thin oil shells; b) after centrifugation and resuspension, the microcapsules were extracted from their oil shells and only traces of oil were found (all scale bars = 100 µm).*

7.3. Cell viability

To assess the compatibility of the phase transfer module with cell encapsulation, cells were encapsulated in 79 µm agarose microcapsules. The cell-laden microcapsules migrated towards the PBS injected phase in the phase transfer module and were collected in an empty tube for 30 minutes. The cell suspension was centrifuged 3 minutes at 217g and the microcapsules were resuspended in 2mL of PBS, to which calcein AM and EthD-1 were added at a concentration of 1µM. The same procedure described before was followed for incubation, rinsing, resuspension and visualization. The results from 6 images each containing 18 cells in average were compiled. It was found that 93 ± 6 % of the cells were alive (in comparison with 92% for the off-chip resuspension procedure). This suggests that cell viability is not affected by the on-chip resuspension procedure.

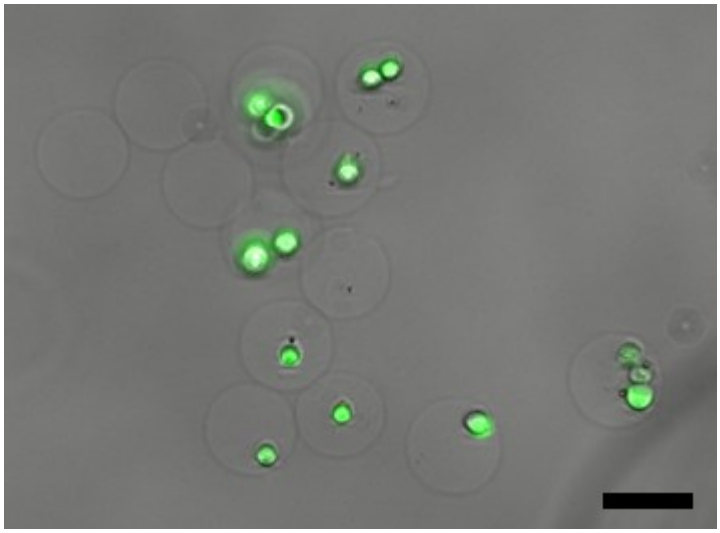

Figure 7-5 *3T3 cells encapsulated in agarose microcapsules and resuspended on-chip yielded a viability of 93 ± 6 %. The phase contrast, green and red fluorescent images were stacked together using ImageJ (scale bar = 80 µm).*

OUTLOOK

As the random encapsulation based on Poisson statistics produces a great number of unoccupied cocoons (~60% for an average cell occupancy of 0.5), future experiments should be directed towards the integration of an on-chip sorting module to isolate the microcapsules containing a single cell. To achieve this, it is necessary to find a physical parameter that varies significantly when a cell is present in a microcapsule. Sorting the microcapsules based on their density was first considered. However, this option is not compatible with the use of a density gradient medium. Because the cells are neutrally buoyant, there is no difference between the density of an unoccupied microcapsule and a cell-laden one. Another alternative is the use of the dielectrophoretic (DEP) force. In the presence of a non-uniform electric field, polarizable particles experience a net force along the field lines. Since the intensity of the force depends on the complex permittivity of the particles, the frequency of the electric field can be adjusted to specifically manipulate different type of particles[82]. Based on this principle, microbeads and cells were successfully separated using DEP force[85]. Consequently, this technique is very promising for the sorting of unoccupied and cell-laden agarose microcapsules.

3T3 cells only constituted a cell model, and the encapsulation of therapeutically relevant cells must now be undertaken. In particular, the encapsulation of endothelial progenitor cells has shown great potential to regenerate ischemic tissues in the case of myocardial infarction and

peripheral vascular disease[20,83]. However, most cells derived from solid mammalian tissues are anchorage-dependent and undergo a specific type of cell death (ie. Anoikis) if they lack matrix support[84]. Furthermore, cell-matrix interaction is needed in some applications of cell-based therapy to promote migration of the cells out of the microcapsules and the engraftment to a specific site[87]. In particular, the incorporation of fibronectin and fibrinogen in agarose microcapsules was shown to enhance the viability and engraftment of marrow stromal cells[20]. Consequently, further work should be geared towards supplementing the agarose microcapsules with proteins that would provide support to the cells. Once long-term cell viability and cell migration have been demonstrated, in vivo animal studies should be performed to assess the engraftment of the cells encapsulated using the proposed method. Finally, cell enhancement via genetic modification is frequently performed in biomedical research. This could also be done on-chip, with the addition of yet another module, this time before the flow focusing geometry[30].

CONCLUSION

Cell-based therapy is promising area of research for the development of new therapeutic strategies. However, despite its great potential for the treatment of many human diseases, cell transplantation is severely limited by low cell survival and retention within the host system. To circumvent these issues, cell encapsulation within picoliter-size polymer networks is routinely used in biomedical research, but the microcapsules generated are typically highly non uniform. Consequently, an array of innovative technologies has been developed to allow the reliable production of size-monodisperse microcapsules. Amongst these techniques, microfluidic platforms offer the unique possibility for reliable semi-automatic lab-on-a-chip processing of the microcapsules.

Ultra-low gelling agarose is commonly used as a biomaterial to constitute the microcapsules because of its great biocompatibility and well characterized properties. Furthermore, agarose microcapsules offer the possibility to encapsulate the cells based on a mild thermoreversible sol-gel transition. Droplet-based microfluidic technologies have been applied to the production of cell-laden agarose microcapsules. However, the microcapsule gelation is typically performed off-chip or at the expense of interrupting the microcapsule production, which is incompatible with additional on-chip downstream processing.

This thesis proposes a method for the uninterrupted production of cell-laden agarose microcapsules with subsequent microcapsule gelation on the same device for applications in cell-based therapy. In order to be relevant for biomedical research, the proposed method is capable of controlled cell encapsulation in uniform microcapsules at a high-throughput and with maintained viability. Furthermore, the capacity of the system for lab-on-a-chip processing is demonstrated by performing cell encapsulation, microcapsule gelation and purification on the same device. Given the success of the proposed method, the platform is now ready to be applied to biomedical research. For this purpose, the agarose microcapsules should be engineered to maximize long-term viability and engraftment of a specific therapeutically relevant type of cell. In particular, endothelial progenitor cells could be used for the regeneration of ischemic tissues.

REFERENCES

1. Asahara, T., Kalka, C. & Isner, J. M. Stem cell therapy and gene transfer for regeneration. *Gene Ther.* **7,** (2000).

2. Dove, A. Cell-based therapies go live. *Nature Biotechnology* **20**, 339-343 (2002).

3. Li, S. C. *et al.* Stem cell engineering for treatment of heart diseases: Potentials and challenges. *Cell Biol. Int.* **33,** 255–267 (2009).

4. Schuler, J. *et al.* Efficacy of prostaglandin E1 in the treatment of lower extremity ischemic ulcers secondary to peripheral vascular occlusive disease. Results of a prospective randomized, double-blind, multicenter clinical trial. *J. Vasc. Surg.* **1**, 160-170 (1984).

5. Lindvall O. *et al.* Grafts of fetal dopamine neurons survive and improve motor function in Parkinson's disease. *Science* **2**, 574-577 (1990).

6. Gage FH. Cell Therapy. *Nature* **392**, 18-24 (1998)

7. Parisi-Amon, A., Mulyasasmita, W., Chung, C. & Heilshorn, S. C. Protein-Engineered Injectable Hydrogel to Improve Retention of Transplanted Adipose-Derived Stem Cells. *Adv. Healthc. Mater.* **2,** 428–432 (2013).

8. Chang, T. M. Semipermeable microcapsules. *Science* **146,** 524–525 (1964).

9. Orive, G., Gascón, A. R., Hernández, R. M., Igartua, M. & Luis Pedraz, J. Cell microencapsulation technology for biomedical purposes: novel insights and challenges. *Trends Pharmacol. Sci.* **24,** 207–210 (2003).

10. Iwata, H. *et al.* Feasibility of agarose microbeads with xenogeneic islets as a bioartificial pancreas. *J. Biomed. Mater. Res.* **28,** 1003–1011 (1994).

11. Hasse, C. *et Al.*, Parathyroid allotransplantation without immunosuppression, *The Lancet* **350**, 1296-1297 (1997).

12. Chang, P. L. *et al.* The in vivo delivery of heterologous proteins by microencapsulated recombinant cells. *Trends Biotechnol.* **17,** 78–83 (1999).

13. Visted, T., Bjerkvig, R. & Enger, P. Ø. Cell encapsulation technology as a therapeutic strategy for CNS malignancies. *Neuro-Oncol.* **3,** 201–210 (2001).

14. Rabanel, J.-M., Banquy, X., Zouaoui, H., Mokhtar, M. & Hildgen, P. Progress technology in microencapsulation methods for cell therapy. *Biotechnol. Prog.* **25,** 946–963 (2009).

15. Vermonden, T. *et al.* Photopolymerized Thermosensitive Hydrogels: Synthesis, Degradation, and Cytocompatibility. *Biomacromolecules* **9,** 919–926 (2008).

16. Hernández, R. M., Orive, G., Murua, A. & Pedraz, J. L. Microcapsules and microcarriers for in situ cell delivery. *Adv. Drug Deliv. Rev.* **62,** 711–730 (2010).

17. *Polysaccharides for Drug Delivery and Pharmaceutical Applications*. **934,** (American Chemical Society, 2006).

18. Iwata, H. *et al.* Agarose for a bioartificial pancreas. *J. Biomed. Mater. Res.* **26,** 967–977 (1992).

19. Sakai, S., Kawabata, K., Ono, T., Ijima, H. & Kawakami, K. Development of mammalian cell-enclosing subsieve-size agarose capsules (<100µm) for cell therapy. *Biomaterials* **26,** 4786–4792 (2005).

20. Karoubi, G., Ormiston, M. L., Stewart, D. J. & Courtman, D. W. Single-cell hydrogel encapsulation for enhanced survival of human marrow stromal cells. *Biomaterials* **30,** 5445–5455 (2009).

21. Rees, D. A. Shapely polysaccharides. The eighth Colworth medal lecture. *Biochem. J.* **126,** 257 (1972).

22. Arnott S. *et al.* The agarose double helix and its function in agarose gel structure. *Journal of Molecular Biology* **90**, 273-284 (1974).

23. Xie, J. & Wang, C.-H. Electrospray in the dripping mode for cell microencapsulation. *J. Colloid Interface Sci.* **312,** 247–255 (2007).

24. Gañán-Calvo, A. M. Generation of steady liquid microthreads and micron-sized monodisperse sprays in gas streams. *Phys. Rev. Lett.* **80,** 285 (1998).

25. Joscelyne, S. M. & Träg\a ardh, G. Membrane emulsification—a literature review. *J. Membr. Sci.* **169,** 107–117 (2000).

26. Gañán-Calvo, A. M. & Gordillo, J. M. Perfectly Monodisperse Microbubbling by Capillary Flow Focusing. *Phys. Rev. Lett.* **87,** (2001).

27. Umbanhowar, P. B., Prasad, V. & Weitz, D. A. Monodisperse Emulsion Generation via Drop Break Off in a Coflowing Stream. *Langmuir* **16,** 347–351 (2000).

28. Whitesides, G. M. The origins and the future of microfluidics. *Nature* **442,** 368–373 (2006).

29. Christopher, G. F. & Anna, S. L. Microfluidic methods for generating continuous droplet streams. *J. Phys. Appl. Phys.* **40,** R319–R336 (2007).

30. Sharei, A. *et al.* A vector-free microfluidic platform for intracellular delivery. *Proc. Natl. Acad. Sci.* **110,** 2082–2087 (2013).

31. Nisisako, T., Torii, T. & Higuchi, T. Novel microreactors for functional polymer beads. *Chem. Eng. J.* **101,** 23–29 (2004).

32. Xu, S. *et al.* Generation of Monodisperse Particles by Using Microfluidics: Control over Size, Shape, and Composition. *Angew. Chem. Int. Ed.* **44,** 724–728 (2005).

33. Chokkalingam, V. *et al.* Optimized droplet-based microfluidics scheme for sol–gel reactions. *Lab. Chip* **10,** 1700 (2010).

34. Niu, X., Gulati, S., Edel, J. B. & deMello, A. J. Pillar-induced droplet merging in microfluidic circuits. *Lab. Chip* **8,** 1837 (2008).

35. Lin, B.-C. & Su, Y.-C. On-demand liquid-in-liquid droplet metering and fusion utilizing pneumatically actuated membrane valves. *J. Micromechanics Microengineering* **18,** 115005 (2008).

36. Choi, J.-H., Lee, S.-K., Lim, J.-M., Yang, S.-M. & Yi, G.-R. Designed pneumatic valve actuators for controlled droplet breakup and generation. *Lab. Chip* **10,** 456 (2010).

37. Jullien, M.-C., Tsang Mui Ching, M.-J., Cohen, C., Menetrier, L. & Tabeling, P. Droplet breakup in microfluidic T-junctions at small capillary numbers. *Phys. Fluids* **21,** 072001 (2009).

38. Song, H., Tice, J. D. & Ismagilov, R. F. A microfluidic system for controlling reaction networks in time. *Angew. Chem.* **115,** 792–796 (2003).

39. Deng, Y. *et al.* Rapid purification of cell encapsulated hydrogel beads from oil phase to aqueous phase in a microfluidic device. *Lab. Chip* **11,** 4117 (2011).

40. Wong, E. H., Rondeau, E., Schuetz, P. & Cooper-White, J. A microfluidic-based method for the transfer of biopolymer particles from an oil phase to an aqueous phase. *Lab. Chip* **9,** 2582 (2009).

41. Ahn, K. *et al.* Dielectrophoretic manipulation of drops for high-speed microfluidic sorting devices. *Appl. Phys. Lett.* **88,** 024104 (2006).

42. Mazutis, L. & Griffiths, A. D. Preparation of monodisperse emulsions by hydrodynamic size fractionation. *Appl. Phys. Lett.* **95,** 204103 (2009).

43. Franke, T., Abate, A. R., Weitz, D. A. & Wixforth, A. Surface acoustic wave (SAW) directed droplet flow in microfluidics for PDMS devices. *Lab. Chip* **9,** 2625 (2009).

44. Eun, Y.-J., Utada, A. S., Copeland, M. F., Takeuchi, S. & Weibel, D. B. Encapsulating Bacteria in Agarose Microparticles Using Microfluidics for High-Throughput Cell Analysis and Isolation. *ACS Chem. Biol.* **6,** 260–266 (2011).

45. Luo, D., Pullela, S. R., Marquez, M. & Cheng, Z. Cell encapsules with tunable transport and mechanical properties. *Biomicrofluidics* **1,** 034102 (2007).

46. Shi, Y. *et al.* High throughput generation and trapping of individual agarose microgel using microfluidic

approach. *Microfluid. Nanofluidics* **15,** 467–474 (2013).

47. Tumarkin, E. *et al.* High-throughput combinatorial cell co-culture using microfluidics. *Integr. Biol.* **3,** 653 (2011).

48. Kumachev, A. *et al.* High-throughput generation of hydrogel microbeads with varying elasticity for cell encapsulation. *Biomaterials* **32,** 1477–1483 (2011).

49. Novak, R. *et al.* Single-Cell Multiplex Gene Detection and Sequencing with Microfluidically Generated Agarose Emulsions. *Angew. Chem. Int. Ed.* **50,** 390–395 (2011).

50. Leng, X., Zhang, W., Wang, C., Cui, L. & Yang, C. J. Agarose droplet microfluidics for highly parallel and efficient single molecule emulsion PCR. *Lab. Chip* **10,** 2841 (2010).

51. Zhang, H., Jenkins, G., Zou, Y., Zhu, Z. & Yang, C. J. Massively Parallel Single-Molecule and Single-Cell Emulsion Reverse Transcription Polymerase Chain Reaction Using Agarose Droplet Microfluidics. *Anal. Chem.* **84,** 3599–3606 (2012).

52. Desbois L. *et al.* 2012. A microfluidic device for on-chip agarose microbead generation with ultralow reagent consumption. *Biomicrofluidics* **6**, 044101 (2012).

53. Thorsen, T., Roberts, R. W., Arnold, F. H. & Quake, S. R. Dynamic Pattern Formation in a Vesicle-Generating Microfluidic Device. *Phys. Rev. Lett.* **86,** 4163–4166 (2001).

54. Anna, S. L., Bontoux, N. & Stone, H. A. Formation of dispersions using 'flow focusing' in microchannels. *Appl. Phys. Lett.* **82,** 364 (2003).

55. Abate, A. *et al.* Impact of inlet channel geometry on microfluidic drop formation. *Phys. Rev. E* **80,** (2009).

56. Edd, J. F. *et al.* Controlled encapsulation of single-cells into monodisperse picolitre drops. *Lab. Chip* **8,** 1262 (2008).

57. Seemann, R., Brinkmann, M., Pfohl, T. & Herminghaus, S. Droplet based microfluidics. *Rep. Prog. Phys.* **75,** 016601 (2012).

58. Lee, W., Walker, L. M. & Anna, S. L. Role of geometry and fluid properties in droplet and thread formation processes in planar flow focusing. *Phys. Fluids* **21,** 032103 (2009).

59. Garstecki, P., Stone, H. & Whitesides, G. Mechanism for Flow-Rate Controlled Breakup in Confined Geometries: A Route to Monodisperse Emulsions. *Phys. Rev. Lett.* **94,** (2005).

60. Nunes, J. K., Tsai, S. S. H., Wan, J. & Stone, H. A. Dripping and jetting in microfluidic multiphase flows applied to particle and fibre synthesis. *J. Phys. Appl. Phys.* **46,** 114002 (2013).

61. Tjahjadi, M., Stone, H. A. & Ottino, J. M. Satellite and subsatellite formation in capillary breakup. *J. Fluid Mech.* **243,** 297–317 (1992).

62. Garstecki, P. *et al.* Formation of monodisperse bubbles in a microfluidic flow-focusing device. *Appl. Phys. Lett.* **85,** 2649–2651 (2004).

63. Garstecki, P., Fuerstman, M. J., Stone, H. A. & Whitesides, G. M. Formation of droplets and bubbles in a microfluidic T-junction—scaling and mechanism of break-up. *Lab. Chip* **6,** 437 (2006).

64. Zagnoni, M. & Cooper, J. M. in *Methods in Cell Biology* **102,** 23–48 (Elsevier, 2011).

65. Chabert, M. & Viovy, J.-L. Microfluidic high-throughput encapsulation and hydrodynamic self-sorting of single cells. *Proc. Natl. Acad. Sci.* **105,** 3191–3196 (2008).

66. Zhang, H., Tumarkin, E., Sullan, R. M. A., Walker, G. C. & Kumacheva, E. Exploring Microfluidic Routes to Microgels of Biological Polymers. *Macromol. Rapid Commun.* **28,** 527–538 (2007).

67. Duffy, D. C., McDonald, J. C., Schueller, O. J. A. & Whitesides, G. M. Rapid Prototyping of Microfluidic Systems in Poly(dimethylsiloxane). *Anal. Chem.* **70,** 4974–4984 (1998).

68. Anderson, J. R., Chiu, D. T., Wu, H., Schueller, O. J. & Whitesides, G. M. Fabrication of microfluidic systems in poly (dimethylsiloxane). *Electrophoresis* **21,** 27–40 (2000).

69. Olivier, J. A., *et Al.*, Reconfigurable diffraction gratings based on elastomeric microfluidic devices, *Sensors and Actuators* **78**, 149-159 (1998).

70. Hillborg, H., *et Al.,* Crosslinked polydimethylsiloxane exposed to oxygen plasma studied by neutron reflectometry and other surface specific techniques, *Polymer* **41**, 6851 - 6863 (2000).

71. Lee, J. N., Park, C. & Whitesides, G. M. Solvent Compatibility of Poly(dimethylsiloxane)-Based Microfluidic Devices. *Anal. Chem.* **75,** 6544–6554 (2003).

72. Holtze, C. *et al.* Biocompatible surfactants for water-in-fluorocarbon emulsions. *Lab. Chip* **8,** 1632 (2008).

73. Baret, J.-C. Surfactants in droplet-based microfluidics. *Lab. Chip* **12,** 422 (2012).

74. Griffin W. C. Classification of surface-active agents by HLB. *Journal of the society of cosmetic chemists, 311-326 (1949).*

75. Martinez, C. J. *et al.* A Microfluidic Approach to Encapsulate Living Cells in Uniform Alginate Hydrogel Microparticles. *Macromol. Biosci.* **12,** 946–951 (2012).

76. Ward, T., Faivre, M., Abkarian, M. & Stone, H. A. Microfluidic flow focusing: Drop size and scaling in pressureversus flow-rate-driven pumping. *ELECTROPHORESIS* **26,** 3716–3724 (2005).

77. Dupin, M., Halliday, I. & Care, C. Simulation of a microfluidic flow-focusing device. *Phys. Rev. E* **73,** (2006).

78. Lulevich V. V. *et al.*Elasticity of polyelectrolyte multilayer microcapsules. *J. Chem. Phys.* **120**, 3822-3826 (2004).

79. Humphries, J. D. Integrin ligands at a glance. *J. Cell Sci.* **119,** 3901–3903 (2006).

80. Huang, H.-L. *et al.* Research Trypsin-induced proteome alteration during cell subculture in mammalian cells. *J. Biomed. Sci.* **17,** 36 (2010).

81. Yu, L. *et al.* Flow-through functionalized PDMS microfluidic channels with dextran derivative for ELISAs. *Lab. Chip* **9,** 1243 (2009).

82. Jones, T. B. Basic theory of dielectrophoresis and electrorotation. *Eng. Med. Biol. Mag. IEEE* **22,** 33–42 (2003).

83. Yuan, Y., Altalhi, W. A., Ng, J. J. & Courtman, D. W. Derivation of human peripheral blood derived endothelial progenitor cells and the role of osteopontin surface modification and eNOS transfection. *Biomaterials* **34,** 7292–7301 (2013).

84. Frisch, S. M. & Screaton, R. A. Anoikis mechanisms. *Curr. Opin. Cell Biol.* **13,** 555–562 (2001).

Appendix I – Protocols

Piranha etch

1. Remove all organic solvents from the fumehood and cover its surface with blue wipes to detect acid spills. Leave the water running at all time for security reasons.

2. Put 200mL of water in a clean 1L beaker labeled “acid waste”.

3. Measure 10mL of H_2O_2. Set it aside.

4. Wearing a protective mask, apron and rubber gloves, measure 30 mL of sulfuric acid and mix it with the H_2O_2 in a glass flat bottom dish contained in a secondary glass dish.

5. Everything that comes in contact with acid should be rinsed thoroughly prior to disposal.

6. Blow dry a silicon wafer and gently place it in the piranha solution.

7. If a second wafer is to be etched, ensure that the first wafer is completely submerged in piranha and place the second wafer gently on top. Shake the acid solution gently to submerge the second wafer.

8. After 15 minutes, shake the acid bath gently once again.

9. After 30 minutes, transfer the wafers into a clean glass dish filled with water three times to ensure complete removal of the acid.

10. Empty the acid in the waste beaker and let it degas through the night.

Making a master mold

1. Choose the proper SU-8 photoresist based on thickness range and get the specifications for the desired channel height on the Microchem website.

2. Start the ventilation system and the electronics for the UV lamp (it takes about 30 minutes to heat up).

3. Blow dry the etched wafer and place them on a hot plate at 200 °C for 4 minutes to dehydrate them. Allow 2 minutes for cool down.

4. Pour photoresist on the wafer and rotate it manually until it is completely covered. Enter the acceleration and duration of the process and initiate spin coating.

5. Soft bake the wafer at 65 °C and 95 °C for the prescribed time.

6. Align the photomask and the wafer using the mask aligner and place the wafer in vacuum contact with the photomask. Expose the photoresist to UV light for the prescribed time.

7. Post-exposure bake the wafer at 65 °C and 95 °C for the prescribed time. Allow 3 minutes for cool down.

8. Submerge the wafer in SU-8 developer for the prescribed time. Gently agitate.

9. Confirm that there is no uncrosslinked SU-8 by applying isopropanol on the wafer.

9. Confirm that the master mold features have a good resolution and are not cracked using a stereomicroscope.

10. Confirm the height of the features using a stylus profiler.

11. Turn off exposure system electronics. Leave the ventilation system running to cool down the UV bulb.

12. Clean the spin coater thoroughly

13. Place the wafer in a vacuum chamber along with 1µL of (Tridecafluoro-1,1,2,2-tetrahydrooctyl)-1-trichlorosilane in a separate dish. Leave under vacuum for 1 hour.

Replica molding of PDMS devices

1. Stick the master mold to the bottom of a petri dish using scotch tape.

2. Weight the base agent and the curing agent of PDMS in a ratio of 10 to 1. Mix both agents thoroughly.

4. Pour the PDMS on the master mold and degas in a vacuum chamber for 30 minutes.

6. Place the master mold in the 80 °C oven for 3 hours to accelerate the curing process.

7. Peel-off the cured PDMS from the master mold using a X-Acto blade.

8. Cut the devices using a X-Acto blade and punch the access holes using a 0.75 mm puncher.

9. To clean the devices, rinse the channel surface with isopropanol, blow dry and apply scotch tape three times. Clean glass slides using the same procedure.

10. Expose the devices and the glass slides to a 30 watts oxygen plasma for 30 seconds.

11. Align the devices and the glass slides and gently press them against each other.

12. Confirm that no debris are obstructing the microfluidic channels and that the channels have not collapsed using the stereomicroscope.

13. Leave the device in the 80 °C oven for 48 hours to ensure complete hydrophobic recovery.

Acidic treatment of the phase transfer module

1. Remove all organic solvents from the fumehood and cover its surface with blue wipes to detect acidic spills. Leave the water running at all time for security reasons.

2. Wearing a protective mask, apron and rubber gloves, mix 1 mL of deionized water, 200 µL of H_2O_2 and 200 µL of HCl in a 3mL glass insert using a polypropylene pipette tip.

3. Place the insert containing the acidic solution inside a 40mL glass vial for pressurization. Connect the tubing to the injection inlet.

4. Fill another 40mL glass vial with deionized water and connect the tubings to the three inlets of the FF geometry.

5. Place a 40mL beaker contain 30 mL of water at the outlet of the microfluidic device.

6. Apply a pressure of 0.04 MPa to the acidic solution and the deionized water. Confirm that both fluids form a laminar interface in the narrow channel. Modify the pressure applied to the deionized water to adjust the position of the interface. Treat the phase transfer module with the acidic solution for 5 minutes.

7. Turn off the pressure of the acidic solution and increase the pressure of the deionized water to 0.2 MPa. Deionized water should now fill the entire device. Rinse for 10 minutes.

8. Let the acid waste degas through the night.

Cell splitting

1. Wear a lab coat and nitrile gloves.

2. Heat the following solutions to 37°C: DMEM culture medium (10% fetal bovine albumin and 1% penicillin/streptomycin), trypsin (0.05 %), Dulbecco's phosphate buffered saline (DPBS, no ca^{2+}/mg^{2+}) and agarose solution.

3. Work under a biological cabinet. Spray everything that enters the biological cabinet with 70 % ethanol.

4. Remove the culture medium from the culture dish and add 10mL of phosphate buffered saline (PBS). Gently agitate.

6. Remove the PBS and add 2mL of trypsin. Incubate for 2 minutes.

7. Confirm the cell dissociation. Add 10 mL of culture medium and transfer the cell suspension to a 15mL falcon tube. Centrifuge at 217g for 3 minutes.

8. Remove the supernatant, and resuspend the cells in 1mL of DPBS.

9. Mix 25 µL of the cell suspension with 25 µL DPBS and measure the cell concentration using a hemocytometer.

10. Calculate the volume of cell suspension corresponding to 1.25×10^5 cells. Plate the 1.25×10^5 cells in a petri dish, add 10mL of culture medium and incubate.

11. Based on the remaining number of cells, calculate the total volume in which the cells should be resuspended to obtain the desired concentration for the cell encapsulation procedure.

12. Centrifuge the cell suspension at 217g for 3 minutes. Remove the supernatant and resuspend in the calculated volume of agarose solution. Vortex 10 seconds at power 8 to resuspend the cells.